Chapter 2

Non-Classical Crystallization of Thin Films and Nanostructures in CVD Process

Jae-soo Jung and Nong-moon Hwang

Additional information is available at the end of the chapter

http://dx.doi.org/10.5772/63926

Abstract

Non-classical crystallization, where crystals grow by the building blocks of nanoparticles, has become a significant issue not only in solution but also in the gas phase synthesis such as chemical vapor deposition (CVD). Recently, non-classical crystallization was observed in solution in-situ by transmission electron microscope (TEM) using a liquid cell technique. In various CVD processes, the generation of charged nanoparticles (CNPs) in the gas phase has been persistently reported. Many evidences supporting these CNPs to be the building blocks of thin films and nanostructures were reported. According to non-classical crystallization, many thin films and nanostructures which had been believed to grow by individual atoms or molecules turned out to grow by the building blocks of CNPs. The purpose of this paper is to review the development and the main results of non-classical crystallization in the CVD process. The concept of non-classical crystallization is briefly described. Further, it will be shown that the puzzling phenomenon of simultaneous diamond deposition and graphite etching, which violates the second law of thermodynamics when approached by classical crystallization, can be approached successfully by non-classical crystallization. Then, various aspects of non-classical crystallization in the growth of thin films and nanostructures by CVD will be described.

Keywords: chemical vapor deposition, non-classical crystallization, thin films, charged nanoparticles, gas phase nucleation

1. Introduction

The theory of classical crystal growth was established based on the concept that the building block of crystals should be individual ions, atoms, or molecules. However, there have been some experimental results, which cannot be properly explained by this classical mechanism. Rather such experimental results strongly imply that crystals should grow by the building blocks of nanoparticles, whose way of crystal growth is called 'non-classical crystallization' [1–5]. Recently, non-classical crystallization was confirmed by in-situ transmission electron microscope (TEM) observations. Although non-classical crystallization is a relatively new and revolutionary concept in crystal growth, it has now become so established that a few related books have been published and its tutorial and technical sessions had been included respectively in the spring meetings of Materials Research Society (MRS) and European Materials Research Society (EMRS) in 2014. With the establishment of non-classical crystallization, many crystals that were believed to grow by atomic, molecular, or ionic entities turn out to grow actually by nanoparticles.

Non-classical crystallization can be applied to crystal growth not only in solution but also in the gas phase synthesis of thin films and nanostructures by chemical vapor deposition (CVD) and physical vapor deposition (PVD). Hwang et al. [6–10] extensively studied non-classical crystallization in the CVD process, publishing more than 80 SCI papers. They suggested that the electric charge carried by the nanoparticles played a critical role, by which the growth of thin films and nanostructures by the building blocks of nanoparticles is made possible. This is why they called this new growth mechanism in the gas phase synthesis 'theory of charged nanoparticles (TCN)'. According to this theory, charged nanoparticles (CNPs), which are spontaneously generated in the gas phase in most CVD processes, contribute to the growth of thin films and nanostructures. If nanoparticles are neutral, they undergo random Brownian coagulation, producing a very porous structure. If nanoparticles are charged, however, they deposit as dense films without voids. This is because CNPs undergo self-assembly and are liquid-like, resulting in epitaxial recrystallization.

There seem to be two reasons why this new growth mechanism has been unknown. The first reason would be that CNPs are invisible because their size is much smaller than the wavelength of visible light. The second reason would be that it is difficult to believe that CNPs can be the building blocks for the evolution of dense films and nanostructures. The generation of CNPs in the gas phase was experimentally confirmed in many CVD processes synthesizing such as diamond [11, 12], ZrO_2 [13], Si [14], carbon nanotubes [15, 16], ZnO nanowires [17], and silicon nanowires [18]. The critical reason why these CNPs can be the building blocks of thin films and nanostructures is that the charge weakens the bond strength and makes nanoparticles liquid-like.

TCN was first suggested to explain the paradoxical experimental observation of simultaneous deposition of less stable diamond and etching of stable graphite. This phenomenon violates the second law of thermodynamics if approached by the classical concept of crystal growth by an atomic unit.

http://dx.doi.org/10.5772/63926

2. Non-classical crystallization

2.1. Theory of charged nanoparticles in CVD

Thin film growth by CVD is explained in text books as follows. Atoms or molecules are formed on the growing surface or in the gas phase as a result of chemical reactions of reactant gases. Those atoms or molecules are then adsorbed on a terrace, diffused to a ledge and become incorporated in the crystal lattice at the kink, which is called the terrace, ledge, and kink (TLK) model [19, 20]. This mechanism is called 'classical crystal growth mechanism'. Normally, a ledge of monoatomic height is regarded as a kink because the ledge is disordered or rough, consisting of lots of kinks. An atom on the terrace, which is called an adatom, has excess broken bonds but an atom at the kink has no excess broken bond. For this reason, a reversible transfer of atoms occurs only at kinks during condensation or evaporation. In other words, the interaction of atoms or molecules with the terrace is repulsive; however, their interaction with the kink is attractive. Because of this difference between the terrace and kink, atoms are only accommodated at the kink, which results in self-assembly of atoms or molecules. If the atomic interaction with the terrace should be attractive as well, there would be no atomic self-assembly, resulting in random packing of atoms and the growing film would become amorphous.

In this paradigm of thin film growth, the maximum supersaturation, which would define the maximum growth rate, would be the one which triggers the onset of gas-phase nucleation. However, according to Hwang et al. [9, 10], the supersaturation that triggers the gas-phase nucleation turns out to be so low that the film growth rate without gas-phase nucleation is negligibly low and such processing conditions would be hardly adopted in the thin film industry. In other words, under the process conditions of commercially available thin films, the gas-phase nucleation occurs in general. This means that thin films are growing inevitably under the condition of gas-phase nucleation in most CVD and PVD processes.

It was believed that the gas-phase nucleation would be harmful to the thin film growth. Gas phase-generated nanoparticles may cause killer defects, resulting in device failure, due to small feature sizes, which decrease to <100 nm [21]. However, Hwang and Lee [10] suggested that the deposition behavior of gas phase-generated nanoparticles differs drastically depending on whether they are electrically charged or not. Neutral nanoparticles produce a porous skeletal structure, usually degrading the property of films. However, CNPs tend to be liquid-like and tend to deposit epitaxially, leaving no voids behind, producing dense films. The film microstructures evolved by the deposition of liquid-like CNPs would be difficult to distinguish from those by the deposition of individual atoms or molecules.

Therefore, in order to grow a high quality film at a high deposition rate, it would be necessary to utilize the generation of CNPs in the gas phase. In accordance with this new understanding, Yoshida et al. [22] could grow high T_c superconducting ($YBa_2Cu_3O_{7-x}$) films epitaxially at a rate as high as 16 nm/s by supplying $YBa_2Cu_3O_{7-x}$ particles using the plasma flash evaporation method. Cabarrocas [23, 24], Vladimirov and Ostrikov [25], and Nunomura et al. [26] also utilize the incorporation of gas phase-nucleated nanoparticles in the plasma-enhanced CVD

(PECVD) process. During the deposition of silicon by PECVD, Cabarrocas [23, 24] deposited polymorphous films, where gas phase-generated crystalline silicon nanoparticles are incorporated into the films. Polymorphous films have better stability and electrical properties than amorphous films.

Crystal growth mechanism by the building blocks of nanoparticles has a long history. For example, more than 40 years ago, Glasner et al. [27–30] suggested that nanometer-sized nuclei were generated in the solution with Pb^{2+} during the growth of KBr and KCl. They confirmed that the crystal was grown by self-assembly of the block nuclei in the solution. The crystallinity increased with decreasing size of nuclei. Sunagawa [31, 32], made a similar suggestion that the growth unit of synthetic diamond is not an atom but a much larger unit. These suggestions were not accepted in the crystal growth community largely because the experimental tools were not available at that time to confirm the generation of nanoparticles in solution or in the gas phase. Besides, it was believed that crystal growth by the building blocks of nanoparticles would produce aggregates of nanoparticles instead of dense structures. For example, Glasner et al. [27–30]'s suggestion was doubted and criticized [33] and has been neglected in the crystal growth community.

Such a way of crystal growth by the building blocks of nanoparticles is now well-established and called 'non-classical crystallization' [34, 35]. **Figure 1** compares crystalline pathways between classical and non-classical crystallization. The building blocks of classical crystallization are atoms, ions, or molecules, which form nanoparticles (**Figure 1(a)**) [35]. As described in the classical nucleation theory, these nanoparticles may grow or shrink by the relative magnitude of surface and bulk energies. If nanoparticles reach the size of the critical nucleus, they can continue to grow into macro crystals by the attachment of an individual atom or molecule.

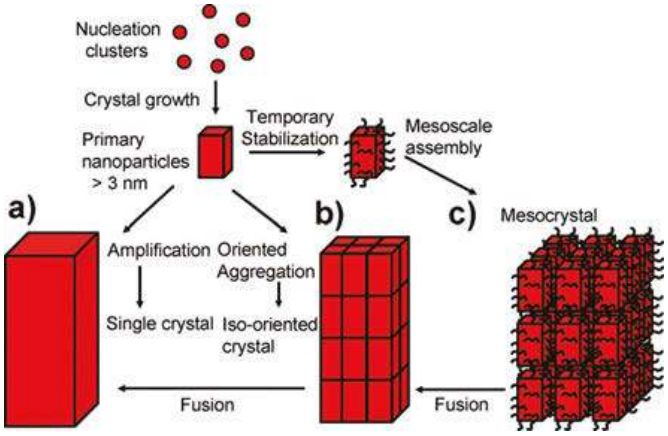

Figure 1. Schematic representation of classical and non-classical crystallization. (a) Classical crystallization. (b) oriented attachment of primary nanoparticles. (c) mesocrystal formation via self-assembly of primary nanoparticles covered with organics. Reprinted with permission from [35]. Copyright 2006 Elsevier.

http://dx.doi.org/10.5772/63926

Figure 1(b) shows the main course of non-classical crystallization, where an iso-oriented crystal grows by oriented attachment of primary nanoparticles, which can form a single crystal upon fusion of the nanoparticles. If the nanoparticles are covered by some organic components, they can form a mesocrystal by mesoscale assembly (path (c)). Cölfen and Antonietti [36] studied a mesocrystal as a superstructure of crystalline nanoparticles with external crystal faces on the scale of hundreds nanometers to micrometers. They also studied that the mesocrystal intermediates can lead to the synthesis of single crystals with included organic additives. During the synthesis process of single crystals, highly oriented nanoparticle-based intermediates could be observed as shown in **Figure 1(c)**. If these mesocrystal intermediates are heated at sufficiently high temperature, they can fuse into a single crystal.

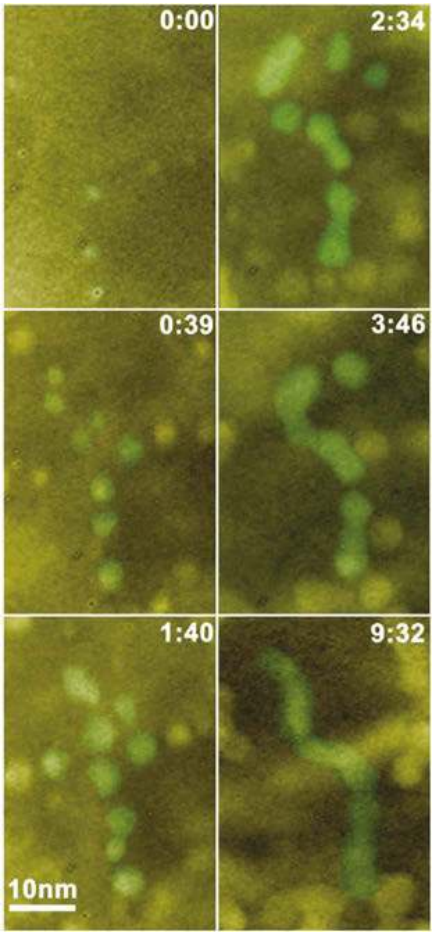

Figure 2. TEM images of the initial nucleation and growth of Pt_3Fe nanowires in the molecular precursor solution. Reprinted with permission from [37]. Copyright 2012 Elsevier.

Figure 1(c) shows that the mesocrystal intermediates clearly reveal the kinetic path of crystallization. Therefore, the mesocrystal intermediates have an important role in revealing the mechanism of non-classical crystallization. However, when the kinetics follows the path of **Figure 1(b)**, it would be difficult to distinguish from a final morphology of the crystal whether it had grown by an individual atom or nanoparticle. This is why crystal growth by nanoparticles had a great resistance in the crystal growth community in the early years.

Recently, crystal growth by nanoparticles in solution could be directly observed by TEM using a liquid cell [37, 38], which provided direction evidences for non-classical crystallization. Liao et al. [37] show detailed real-time imaging to show how Pt_3Fe nano-rods grow by nanoparticles in solution using a silicon nitride liquid cell for in situ TEM observation.

Figure 2 shows images listing the growth process of a twisted Pt_3Fe nanowire. In the initial stage of growth, many small nanoparticles are formed when the Pt and Fe precursors are reduced by electron beam illumination. Some of them grow by monomer attachment and others undergo coalescence. The nanoparticles were combined by coalescence and then relaxed into nanoparticles. Finally, the average size of these nanoparticles reached 5.3 ± 0.9 nm.

In the second stage, nanoparticles interact with each other to form nanoparticle chains. The nanoparticle chain is formed by shape-directed nanoparticle attachment with successive structural relaxation into straight Pt_3Fe nano-rods and reorientation, revealing critical mechanisms of the growth into nano-rods from nanoparticle building blocks. Therefore, even when nanoparticles attach without orientation, single-crystalline nano-rods are formed eventually. In the first stage of growth, nanoparticles meet each other, and form dimer. But if the dimer meets another nanoparticle, unlike the first stage of growth, the dimer does not coalesce into a sphere but forms a trimer by connecting the particle to the dimer end. The additional end-to-end attachments generate a nanoparticle chain.

By in situ TEM observation using graphene liquid cells, Yuk et al. [38] carried out direct atomic-resolution imaging to show how Pt crystals grow in solution. The microscope is operated at 80 kV with a beam intensity of 10^3 to 10^4 A/m^2 maintained during nanocrystal growth. Upon locating a liquid pocket on the TEM grid, the beam intensity is optimized, which reduces the Pt precursor and initiates nanocrystal growth [39]. The use of graphene liquid cells made it possible to discern colloidal Pt nanoparticles with radii as small as 0.1 nm and to track their motion, which was not possible by previous cells with silicon nitride windows [39].

Figure 3 shows the TEM images of the nanocrystals which are connected by a neck at the initial stage of coalescence. Neck growth occurs simultaneously with decreasing length (l) and thickness (t), which means that the atoms migrate to the neck region by surface diffusion [40]. After coalescence, the nanocrystal structure gradually reorganizes, evolving truncated surfaces.

Figure 3 shows the detailed process how crystalline growth occurs by the building blocks of nanocrystals. Yuk et al. [38] mentioned in the supporting information that all images were collected under ambient conditions at 23°C. It should be noted that such enhanced kinetics of liquid-like coalescence at such a low temperature can never be expected from neutral

http://dx.doi.org/10.5772/63926

nanocrystals. Although the authors did not mention the role of charge, it should be noted that charging is unavoidable during TEM observation.

According to Hwang and Lee [10], the role of charge is critical in non-classical crystallization since it makes CNPs liquid-like. The liquid-like property of CNPs was deduced by Hwang et al. from the experimental observation that dense films are evolved by the deposition of CNPs. Considering that CNPs are liquid-like, it is expected that the bond strength should be weakened by the presence of charge. To check this possibility, we made an extensive literature survey and found the paper by Clare et al. [41], who studied the effect of charge on the bond strength in hydrogenated amorphous silicon. The main result of this paper and its implications are summarized in the following section.

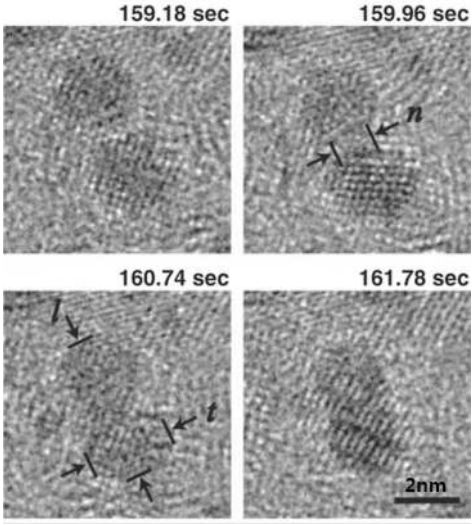

Figure 3. Pt nanocrystal dynamics of coalescence. l, t, and n in the figure represent respectively the length along the center-to-center direction, the thickness in vertical direction to the length and the neck diameter. Reprinted with permission from [38]. Copyright 2012 Elsevier.

2.2. Effect of charge on the bond strength

The effect of a single negative or positive charge on the strength of silicon-silicon and silicon-hydrogen bonds in the molecules SiH_4 and Si_2H_2 was calculated by ab initio calculations. To determine the difference in the energy to break a single Si-H bond in SiH_4, SiH_4^+ and SiH_4^- calculations were done on six species: SiH_3, SiH_4, SiH_3^-, SiH_4^-, SiH_3^+, and SiH_4^+ and the required energies were determined by comparing the bond strength of each species. Similar calculations were done with the species Si_2H_6, Si_2H_5, $Si_2H_6^-$, $Si_2H_5^-$, $Si_2H_6^+$, and $Si_2H_5^+$ to observe the effect of a lower charge/size ratio and to examine the effect of charge on the Si-Si bond energy. The results of ab initio calculations are shown in **Table 1**.

When the atoms are embedded in a lattice, they will not be free to attain geometries resembling the optimized ion geometry, although they will be able to relax to some degree. Thus, the actual effects of charge on bond strength in hydrogenated amorphous silicon will be between those indicated by the unoptimized (adiabatic) and optimized (vertical) rows of **Table 1**. They are likely to be closer to those for the unoptimized rows.

Both positive and negative charges drastically weaken the bond strength of Si-Si and Si-H. The bond strength of Si-Si is weakened from 3.2 eV to 1.11 eV when Si_2H_6 is negatively charged. It is weakened to 1.6 eV when Si_2H_6 is positively charged. The bond strength of Si-H is weakened drastically from 3.9 eV to 0.98 eV when SiH_4 is negatively charged. It is weakened to 0.3 eV when SiH_4 is positively charged.

Compound	Si–H (eV)	Si–Si (eV)
SiH_4 (optimized)	3.9	—
SiH_4^- (optimized)	0.98	—
SiH_4^+ (optimized)	0.30	—
Si_2H_6 (optimized)	3.5	3.2
$Si_2H_6^-$ (optimized)	1.02	1.11
$Si_2H_6^+$ (optimized)	1.59	1.6
SiH_6^- (unoptimized)	1.35	—
SiH_4^- (unoptimized)	0.09	—
$Si_2H_6^-$ (unoptimized)	1.34	1.3
$Si_2H_6^+$ (unoptimized)	1.49	1.6

Table 1. Calculated bond strengths of Si-H and Si-Si. Reprinted with permission from [41]. Copyright 1993 Elsevier.

The effect of charge on the bond strength can be explained by a bond order in the molecular orbital theory. A bond order, which represents the strength or stability of bond, is the number of bonding electron pairs shared by two atoms in a molecule. A bond order is defined as half the difference between the number of bonding electrons and the number of antibonding electrons as expressed by the following equation,

$$\text{Bond order} = \frac{\#of\ bonding\ electrons - \#of\ antibonding\ electrons}{2} \tag{1}$$

If a nanoparticle is charged negatively, electrons are added to the antibonding orbital. If a nanoparticle is charged positively, electrons are removed from the bonding orbital. Therefore, both positive and negative charges would decrease the bond order and thereby weaken the bond strength.

Weakening of bond strength by charge has very important implications because it means that diffusion or kinetics is enhanced. The new concept of charge-induced weakening of bond

strength can explain the liquid-like property of CNPs, which was suggested by Hwang et al. [10]. This concept can also explain the rapid kinetics of coalescence in **Figures 2** and **3**. The concept of charge-enhanced kinetics can explain the enhanced chemical reactions of reactant gases even at low temperature in the PECVD process. It also explains the deposition of crystalline films at low temperature.

Moreover, there are many processes where ion or electron beams are used to enhance the kinetics at low temperature. For example, high quality films can be grown at low temperature by ion-beam-assisted deposition (IBAD) in the sputtering or evaporation processes. Also, there is a process called gas-mediated electron or ion-beam-induced deposition and etching, where beams of electrons and ions are used to modify a surface locally at micron and submicron dimensions or fabricating in three dimensions [42–44]. In all these processes, the enhanced kinetics is not clearly understood, vaguely explained by the bombarding energy of ions or electrons. However, it is highly probable that the enhanced kinetics should come from weakening of the bond strength by charge. Moreover, the effect of charge on weakening the bond strength and thereby enhancing the kinetics seems to be very general, even related with the catalytic effect and the enzyme activity in biology.

Zheng et al. [45] observed the superplastic deformation behavior of nanoscale amorphous silica near room temperature using in situ experiments inside a TEM with low beam intensities without obvious rise in sample temperature. They called the phenomenon electron-assisted superplasticity. After imaging for the positioning of the sample and the diamond flat punch, the beam was blocked with the condenser lens aperture, and the silica particle was compressed with the Hysitron Pico-indenter [46, 47]. The particle is plastically deformed because of the e-beam irradiation it had experienced during the imaging. After ~40% compression [46], where the contact pressure is estimated to be 9.2 GPa, the beam was brought on the sample to image the particle. On unloading, the total plastic percent compression was 27%. On compressive loading again with the beam on, surprisingly, the plastic flow of the glass was continuous and smooth, with no sign of shear banding or cracking. Much easier flow was observed with the ensuing beam-on deformation in a second set of in situ experiments, resulting in a pancake shape. Although the contact area kept increasing, the forces required to deform were at levels considerably lower than those in the beam-off condition. This phenomenon of electron-assisted superplasticity might also be explained by weakening of bond strength by charge.

3. Non classical crystallization in diamond deposition at low pressure

The concept that thin films grow by the building blocks of CNPs was first suggested in the low pressure synthesis of diamonds by Hwang et al. [7]. In this section, it will be briefly reviewed how the TCN was developed as the growth mechanism of diamonds in its low pressure synthesis.

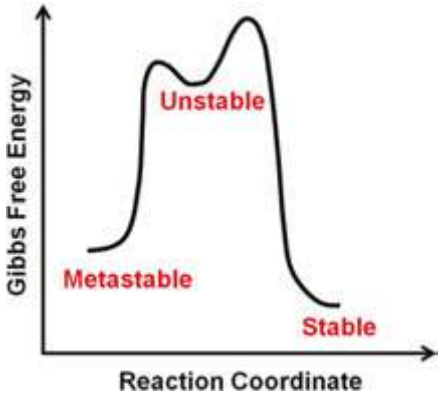

Figure 4. Thermodynamic and kinetic description of the metastable diamond formation. Reprinted with permission from [10]. Copyright 2010 Elsevier.

Low pressure deposition of diamond was reported by pioneering scientists Derjaguin and Fedoseev [48], Spitsyn et al. [49] in HWCVD and Matsumoto et al. [50] in PECVD. Although its process has been studied in depth [51–54], the underlying principle has not been clearly understood. The fundamental question is why diamond can be deposited at low pressure whereas graphite is more stable than diamond.

This question can be explained by **Figure 4** [10]. **Figure 4** describes the general thermodynamic and kinetic explanation of the case where the metastable phase can be formed more dominantly than the stable phase The Gibbs free energy of the stable phase is lower than that of the metastable phase. This difference in free energy determines the difference in the driving force of formation. In other words, the driving force for the formation of the stable phase from the unstable phase is higher than that of the metastable phase.

However, the kinetic barrier, such as a nucleation barrier, is a more important factor that determines the tendency of the formation since the formation of the stable and the metastable phases is a kinetically parallel process. The formation of metastable diamond at low pressure might be explained by this concept. To check this possibility, the nucleation barrier between graphite and diamond should be compared. The Gibbs free energy of nucleation is composed of the driving force for precipitation and the surface energy of the nucleus. Isotropic surface energies of diamond [55] and graphite [56] are respectively 3.7 J/m^2 and 3.1 J/m^2. Since the surface energy of graphite is smaller than that of diamond and the driving force for the precipitation of graphite from the gas phase is larger than that of diamond, the total Gibbs free energy of diamond is higher than that of graphite in all ranges of radius as shown in **Figure 5(a)**. Diamond is less stable than graphite in all ranges of radius in **Figure 5(a)**. Considering only **Figure 5(a)**, it appears that the formation of diamond at low pressure cannot be approached by the concept of the metastable phase formation of **Figure 4**. However, **Figure 5(a)** does not correctly compare the Gibbs free energy between diamond and graphite because the comparison should be made with respect to the number of atoms as shown

http://dx.doi.org/10.5772/63926

in **Figure 5(b)** [57] instead of being made with respect to the radius. Although the surface energy of diamond is larger than that of graphite, the molar volume of diamond (3.41 cm^3/mole) is much smaller than that of graphite (5.405 cm^3/mole). Therefore, the surface energy multiplied by the molar area for diamond (8.38×10^{-4} J) is smaller than that for graphite (9.55×10^{-4} J).

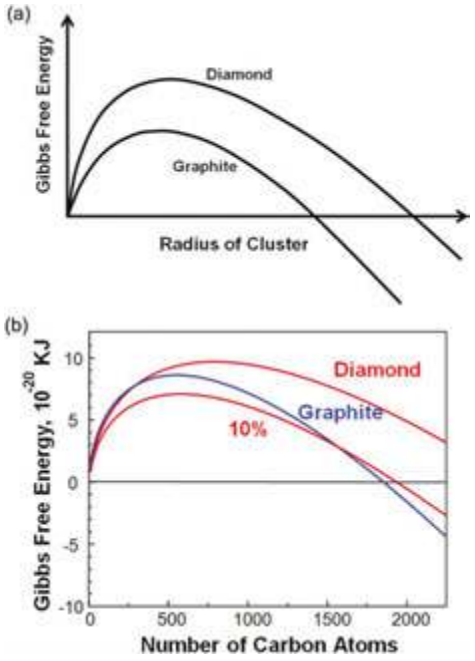

Figure 5. (a) Dependence of Gibbs free energy on the radius of diamond and graphite nanoparticle. (b) Dependence of Gibbs free energy on the number of carbon atoms for diamond and graphite. Reprinted with permission from [57]. Copyright 1997 Elsevier.

The number of atoms at which the Gibbs free energies of diamond and graphite intersect as shown in **Figure 5(b)** can be derived as,

$$n^* = 36\pi \left(\frac{\sigma_{dia} \left(\Omega_{dia}\right)^{\frac{2}{3}} - \sigma_{gra} \left(\Omega_{gra}\right)^{\frac{2}{3}}}{\Delta\mu^{dia \to gra}} \right)^3 \tag{2}$$

where σ_{dia} and σ_{gra} are respectively the surface energies of diamond and graphite, $\boldsymbol{\Omega}_{dia}$ and $\boldsymbol{\Omega}_{gra}$ respectively the atomic volumes of diamond and graphite, and $\Delta\mu_{dia \to gra}$ the free energy difference per atom between diamond and graphite. The reported surface energies of diamond and graphite are 3.7 Jm^{-2} and 3.1 Jm^{-2}, respectively. The chemical potential difference between

diamond and graphite, $\Delta\mu_{dia\rightarrow gra}$, at 927°C is calculated to be -1.2101×10^{-20} J/atom. From these values, n^* for (Eq. 2) is estimated to be 351. This means that for a nucleus containing less than 351 atoms, diamond is more stable than graphite. Although the nucleation curves in **Figure 5(b)**, which are evaluated from the reported surface energy data of some uncertainty, have uncertainties, they definitely tell that diamond can be more stable than graphite for a sufficiently small size. In **Figure 5(b)**, the nucleation barrier of diamond is slightly larger than that of graphite, indicating that graphite would nucleate more dominantly than diamond. However, it should be noted that the difference of the nucleation barrier between diamond and graphite is rather small. If the nucleation barrier of diamond was slightly smaller than that of graphite, diamond synthesis at low pressure would be much easier than now and gas activation such as hot filament and plasma would not be necessary. Oxygen-deficient burning of any carbon-containing materials such as coals, fuels, and woods might have produced diamonds instead of soot.

In reality, graphitic or amorphous carbon is formed without gas activation. It is known that gas activation is essential to the low-pressure synthesis of diamond. If we assume that the role of gas activation is to reduce the surface energy of diamond, the nucleation of diamond can be more dominant than that of graphite. For example, if the gas activation reduces the surface energy of diamond by 10%, n^* in (Eq. 2) becomes 1784 at 927°C, and the nucleation barrier of diamond becomes lower than that of graphite as shown in **Figure 5(b)**.

Hwang et al. [7, 58] suggested that the essential role of gas activation is to generate an abundant amount of electric charge rather than atomic hydrogen and that the negative charge stabilizes diamond over graphite. They further suggested that charged diamond nanoparticles are generated in the gas phase, becoming the building blocks of diamond films. They reached this conclusion from the fact that the well-established experimental observation of simultaneous diamond deposition and graphite etching violates the second law of thermodynamics if diamond deposition occurs by individual atoms.

However, in the diamond CVD community, the 'atomic hydrogen hypothesis', which was suggested by Spitsyn et al. [49], has been the most popular explanation for diamond growth at low pressure. According to the hypothesis, atomic hydrogen, which is produced by gas activation such as hot filament or plasma, etches graphite much faster than diamond and therefore low-pressure synthesis of metastable diamond is possible. This hypothesis is equivalent to saying that even though diamond is less stable than graphite, diamond can grow dominantly over graphite in the presence of atomic hydrogen.

However, this statement violates the second law of thermodynamics because if stable graphite etches away, less stable diamond must etch away. Although the atomic hydrogen hypothesis has a significant drawback of violating the second law of thermodynamics as to the irreversible transfer of carbon atoms [7], it is widely accepted in the diamond CVD community largely because simultaneous diamond deposition and graphite etching are experimentally observed. In other words, the experimental observation appears to violate the second law. This is a very interesting situation. Great attention should be paid to this seeming contradiction between the experimental observation and the second law because it is expected that if such a contradiction is solved, a big discovery may be made.

http://dx.doi.org/10.5772/63926

Let's make a rigorous thermodynamic analysis of the simultaneous diamond deposition and graphite etching. The criterion for the irreversible transfer of atoms between the system and the surrounding, which corresponds to an open system in thermodynamics, is the chemical potential. Chemical potential is defined as the partial derivative of the Gibbs free energy with respect to the number of atoms under constant temperature and pressure [59]. The total Gibbs free energy is decreased when atoms transfer from a phase with high chemical potential to a phase with low chemical potential.

Since graphite is more stable than diamond at the given temperature and pressure of the CVD process according to the phase diagram of carbon [47, 48], the chemical potential of carbon in diamond is higher than that in graphite, which can be written as,

$$\mu_c^{dia} > \mu_c^{gra}, \tag{3}$$

where the subscript *'C'* and the superscripts *'dia'* and *'gra'* mean carbon, diamond, and graphite, respectively. Since reversible etching and deposition are not driven by the difference of the chemical potential and do not produce a net flux, the reversible etching and deposition can occur simultaneously. On the other hand, irreversible etching or deposition is driven by the chemical potential difference and produces a net flux. The irreversible etching and deposition cannot occur simultaneously.

The experimental observation of simultaneous diamond deposition and graphite etching indicates that the chemical potential of carbon in diamond is lower than that in gas and that the chemical potential of carbon in graphite is higher than that in gas. The irreversible graphite etching can be written as

$$\mu_c^{gra} > \mu_c^{gas}, \tag{4}$$

where the superscript *'gas'* represents the gas phase. Similarly, the irreversible diamond deposition can be written as

$$\mu_c^{gas} > \mu_c^{dia} \tag{5}$$

In this paper, etching and deposition refer to the irreversible process and from now on, those words will be used without the adjective 'irreversible'. The simultaneous diamond deposition and graphite etching indicate that Eqs. (4) and (5) should be simultaneously satisfied and can be written as

$$\mu_c^{gra} > \mu_c^{gas} > \mu_c^{dia}, \tag{6}$$

Therefore, the chemical potential of carbon in graphite is larger than that in diamond, which is identical to saying that diamond is more stable than graphite. This contradicts with Eq. (3). Therefore, it is quite evident that the simultaneous diamond deposition and graphite etching or the atomic hydrogen hypothesis violates the second law of thermodynamics.

The contradiction becomes more evident if chemical potentials of carbon for different phases are represented in diagrams as shown in **Figure 6**. **Figure 6** compares chemical potentials of carbon for graphite, diamond, and gas based on the carbon phase diagram (**Figure 6(a)**) and the atomic hydrogen hypothesis or the experimental observation of simultaneous diamond deposition and graphite etching (**Figure 6(b)**).

In the interpretation of this paradoxical observation by the atomic hydrogen hypothesis, it is implicitly assumed that the unbalanced etching rate between graphite and diamond can change the stability between graphite and diamond. This hypothesis neglects the fact that thermodynamic stability is not affected by kinetics. It should be noted that the thermodynamic stability determined by the Gibbs free energy is a state function, which depends only on the initial and final states, not on the kinetic path.

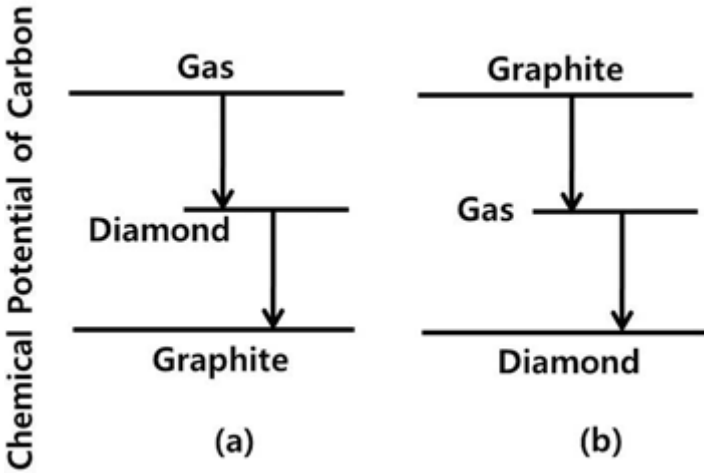

Figure 6. (a) Chemical potentials of carbon for different phases and the direction of carbon atoms indicated by the carbon phase diagram and (b) those indicated by simultaneous diamond deposition and graphite etching based on the assumption that the building block should be an individual atom. Reprinted with permission from [10]. Copyright 2010 Elsevier.

Since the second law of thermodynamics cannot be violated, there must be some logical error in interpreting the experimental observation of simultaneous diamond deposition and graphite etching. What would be the logical error? One thing that should be noted is that etching of diamond and graphite occurs under the condition where the concentration of CH_4 is high enough to deposit both phases. In order to understand this situation, let's consider the phase diagram of the C-H system as shown in **Figure 7** [6].

http://dx.doi.org/10.5772/63926

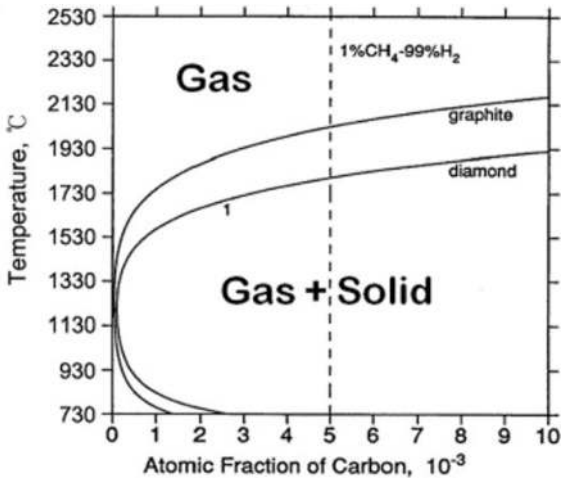

Figure 7. Phase diagram of the C–H system under 2700 Pa. The graphite and diamond lines indicate the maximum solubility of carbon in the gas phase. Reprinted with permission from [6]. Copyright 1996 Elsevier.

The vertical dashed line is for the composition of 1% CH_4-99% H_2, which is typically used in the gas-activated diamond CVD process. At the substrate temperature around 1200 K (927 °C), the vertical line is inside the two-phase region of gas + solid, which means that both diamond and graphite have a driving force for precipitation. This prediction is opposite to the experimental observation of graphite etching. This disagreement between the phase diagram and the experimental observation comes from the implicit assumption that the gas-phase nucleation does not take place. If gas-phase nucleation takes place, the equilibrium carbon content in the gas phase follows the solubility line in **Figure 7**. If diamond nucleates in the gas phase, the carbon content in the gas phase would be the solubility line for diamond. If graphite nucleates in the gas phase, the carbon content in the gas phase would be the solubility line for graphite. Carbon solubility in graphite is lower than that in diamond because graphite is more stable than diamond. This solubility tends to be minimum at ~1300 K and increases with decreasing temperature; it has a retrograde solubility. If diamond or graphite nucleates in the gas phase, carbon in the gas phase would be depleted. When this carbon-depleted gas approaches the substrate, at the temperature of which equilibrium carbon solubility is much higher, etching occurs for both diamond and graphite.

Therefore, the experimental observation of graphite etching indicates that the gas-phase nucleation of diamond or graphite occurred. Besides, in order to explain the experimental observation of simultaneous diamond deposition and graphite etching without violating the second law of thermodynamics, the nuclei should have a diamond structure and at the same time those diamond nuclei should be the building blocks of the growing diamond. According to this scenario, both diamond and graphite are etched away by the atomic unit but diamond deposition occurs by the building block of gas phase-nucleated nanoparticles. This scenario is free from the thermodynamic paradox. Therefore, the puzzling phenomenon of simultaneous

diamond deposition and graphite etching provides strong evidence that diamond deposition should occur by the building blocks of gas phase-nucleated nanoparticles.

To check this scenario, the gas-phase nucleation in the diamond CVD system must be experimentally confirmed. To confirm the existence of CNPs generated in the gas phase, Jeon et al. [11] attached an energy analyzer combined with a Wien filter to the diamond hot filament CVD (HFCVD) reactor. Since the processing pressure in diamond HFCVD is higher than the required pressure for Wien filter measurements, differential pumping was done through an orifice (1.2 mmØ) and a skimmer (2 mmØ) between the measuring chamber and the CVD reactor. By such a system, they could measure the size distribution of negatively charged carbon nanoparticles in the gas phase shown in **Figure 8** [11]. The processing condition of measurement was a gas mixture of 1.5% CH_4–98.5% H_2, a reactor pressure of 800 Pa, and a wire temperature of 2100°C. The peak occurred at ~3000 atomic mass units, which corresponds to ~250 carbon atoms. Based on the negative current measured on the Faraday cup, they estimated the number density of negatively charged nuclei as $\sim 10^6$ mm^{-3}.

Figure 9 shows the paradox-free direction of carbon flux before and after gas-phase nucleation [10]. Before gas-phase nucleation, the gas phase is supersaturated and the driving force is for the deposition of both diamond and graphite (**Figure 9(a)**). On the other hand, after gas-phase nucleation, the gas phase is undersaturated and the driving force is for etching of both diamond and graphite (**Figure 9(b)**). After gas-phase nucleation, however, the gas phase is undersaturated and has the driving force for etching of both diamond and graphite (**Figure 9(b)**). Since both diamond and graphite are etched away by the atomic unit under such conditions, the atomic contribution to diamond growth is negative. Nevertheless, diamond crystals grow under such conditions. This means that the growing diamond is contributed 100% by the building blocks of gas-phase nucleated diamond nanoparticles, whereas the diamond film

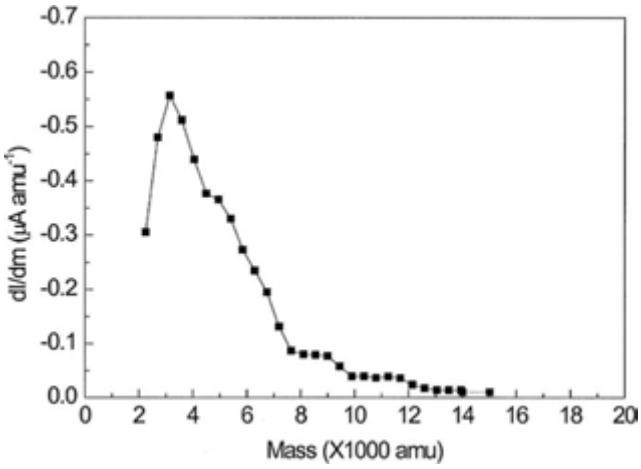

Figure 8. Mass distribution of negatively charged carbon nanoparticles generated in the HWCVD reactor. Reprinted with permission from [11]. Copyright 2000 Elsevier.

http://dx.doi.org/10.5772/63926

deposited on the substrate is being etched atomically. In order for diamond films to grow by the building blocks of CNPs, it must be assumed that CNPs should undergo self-assembly and epitaxial recrystallization. And in order to undergo epitaxial recrystallization, CNPs should be liquid-like. This liquid-like property would come from the weakening of bond strength by charge as explained in the previous section.

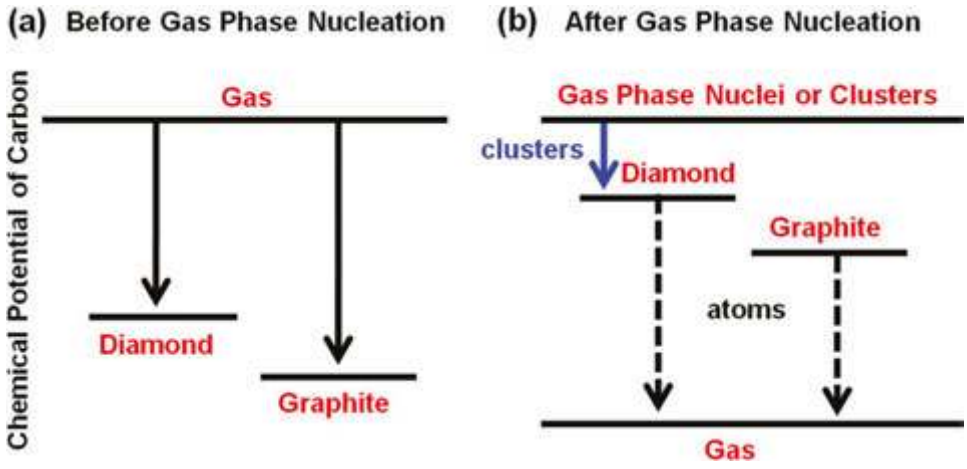

Figure 9. The chemical potentials diagram of carbon in the diamond, graphite, and gas phases before and after gas-phase nucleation. Reprinted with permission from [10]. Copyright 2010 Elsevier.

On the other hand, there is another puzzling phenomenon in the diamond CVD process: under the same deposition condition where diamond films grow on a silicon substrate, highly porous skeletal graphitic soot particles grow on an iron substrate and carbon nanotubes grow on a palladium substrate as shown in **Figure 10** [7, 61]. These results imply that the deposition mechanisms of diamond, soot, and carbon nanotubes should be closely related to one another.

From the previous analysis based on **Figures 4–9**, we know that diamond nucleates in the gas phase. Besides, **Figure 8** confirms that these nuclei are negatively charged. If this knowledge is combined with **Figure 10**, negatively charged diamond nuclei deposit as a diamond film, soot, and carbon nanotubes respectively on silicon, iron and palladium substrates. Since etching takes place atomically, the building blocks of the diamond film, soot, and carbon nanotubes must be negatively charged nanoparticles. In relation with this effect of the substrate, Huh et al. [61] studied the correlation between the deposition behavior and the charge transfer rate of the substrate and found out that there exists an almost perfect correlation that the substrate with a low charge transfer rate produces diamond whereas the substrate with a high charge transfer rate produces soot or carbon nanotubes.

According to Hwang et al. [7], when negatively charged diamond nuclei approach the silicon substrate which has a low charge transfer rate, they maintain a diamond phase and undergo

self-assembly like nano-colloids and epitaxial recrystallization, producing the diamond film as shown in **Figure 10(a)**. However, when they approach the iron substrate, which has a high charge transfer rate, they lose charge to the iron substrate just before landing and transform to graphite. And the neutral graphite nanoparticles make random Brownian aggregations and produce porous skeletal soot on the iron substrate as shown in **Figure 10(b)**. In this scenario, the stability of diamond comes from charge. In other words, when carbon nanoparticles are charged, they have a diamond structure; otherwise, they have a graphite structure. In order to confirm the effect of charge on the stability of diamond, Hwang et al. [7] compared the deposition behavior between floating and grounded iron substrates after 2 hours of deposition. On the grounded iron substrate, soot particles continued to grow. On the floating iron substrate, however, diamond crystals were grown on the initially formed soot particles.

TEM observation of the soot particles by Huh et al. [61] revealed that iron nanoparticles are trapped inside each soot particle. In other words, each soot particle encloses an iron nanoparticle three dimensionally like an onion. If iron nanoparticles are not enclosed three dimensionally by carbon, it might be possible that carbon nanotubes grow. From the fact that carbon nanotubes are evolved on the palladium substrate as shown in **Figure 10(c)**, an insight can be drawn as to the growth mechanism of carbon nanotubes [62]. One possible driving force for the growth of one-dimensional carbon would be the reduction of the electrostatic energy. This possibility is supported by the bias effect on the growth of carbon nanotubes reported by Lee and Hwang [63]. They found out that carbon nanotubes grow only when the substrate is positively biased in the hot filament CVD process using a high methane concentration of 20% CH_4–80% H_2. This possibility is further supported by the experimental observation that one-dimensional carbon such as carbon nanotubes or carbon fibers grow when the catalytic metal nanoparticles are placed on the insulating substrate such as glass, but do not grow when they are placed on the conducting substrate [64].

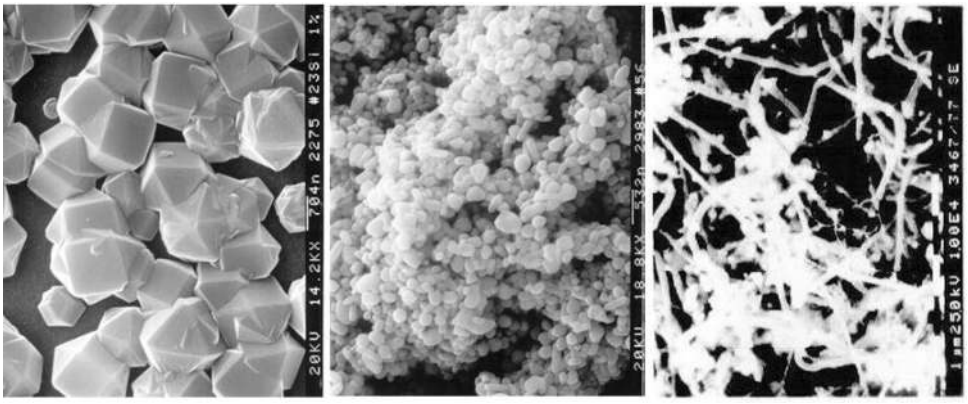

Figure 10. (a) Diamond, (b) soot, and (c) carbon nanotubes grown respectively on Si, Fe, and Pd substrates. Reprinted with permission from [7, 61]. Copyright 1996 Elsevier.

http://dx.doi.org/10.5772/63926

4. Deposition behavior and analysis of non-classical crystallization in the CVD process

4.1. Comparison of deposition behavior between floating and grounded substrates in the silicon CVD process

The generation of CNPs in the gas phase was experimentally confirmed using a differential mobility analyzer (DMA) in many CVD systems [16, 17, 65]. Hwang et al. [9, 10] suggested that these CNPs are the building blocks of thin films and nanostructures in most CVD processes. Experimental confirmation of CNPs in the gas phase is not sufficient to say that they are the building blocks. However, the Si-Cl-H system has retrograde solubility like the C-H system [66]. Besides, in the CVD of the Si-Cl-H system, a paradoxical phenomenon of simultaneous deposition and etching of silicon was reported [67]. This phenomenon also violates the second law of thermodynamics if the silicon film grows by individual atoms. In order to avoid the violation, the charged silicon nuclei formed in the gas phase should be the building blocks of growing silicon films [9, 10].

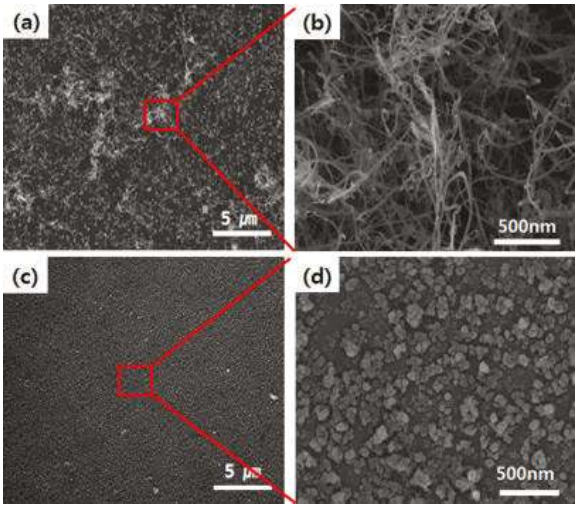

Figure 11. FESEM images: (a) low-magnification and (b) high-magnification images of a floating silicon substrate and (c) low-magnification and (d) high-magnification images of a grounded silicon substrate at a N_2 flow rate of 500 sccm. Reprinted with permission from [64]. Copyright 2014 Elsevier.

In order to show CNPs to be building blocks of thin films or nanostructures in a silicon CVD process, Youn et al. [64] compared the deposition behavior between floating and grounded silicon substrates. Charge build-up would be maximized on the floating substrate and minimized on the grounded substrate. The result is shown in **Figure 11**.

Figure 11(a) and **(b)** shows respectively low- and high-magnification FESEM images of the surface microstructure of the floating substrate after deposition for 2 hours. The substrate

temperature is 900°C and the gas flow rates are 5 sccm 10% SiH_4–90% He, 50 sccm H_2, and 500 sccm N_2. **Figure 11(c)** and **(d)** shows respectively low- and high-magnification FESEM images of the surface microstructure of the grounded substrate with the deposition conditions being the same as those of **Figure 11(a)** and **(b)**. Silicon nanowires grew extensively on the floating substrate as shown in **Figure 11(a)** and **(b)**, whereas no silicon nanowire grew but only silicon nanoparticles were deposited on the grounded substrate as shown in **Figure 11(c)** and **(d)**. Diameters of the nanowires in **Figure 11(b)** are about 10–30 nm. In **Figure 11(b)**, without catalytic metals or seeds of silicon oxide, silicon nanowires were grown on the substrate. Neither vapor-liquid-solid (VLS) [68] nor oxide-assisted growth (OAG) [69] mechanism can explain this deposition behavior.

Floating and grounding of the substrate are the only differences in the processing condition between **Figure 11(b)** and **(d)**. Therefore, charge build-up would be the only difference between **Figure 11(b)** and **(d)**. Considering this, the growth of silicon nanowires would be attributed to the charge build-up. In other words, the electrostatic interaction between the CNPs and the substrate is responsible for the growth of the silicon nanowires.

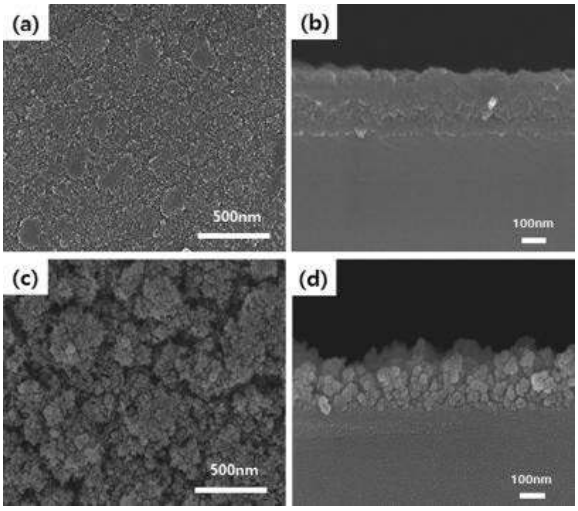

Figure 12. FESEM images for (a) plane view and (b) cross section of films deposited on a floating silicon substrate and (c) plane view and (d) cross section of films deposited on a grounded silicon substrate at a N_2 flow rate of 1000 sccm. Reprinted with permission from [64]. Copyright 2014 Elsevier.

When the N_2 flow rate was increased from 500 sccm to 1000 sccm, films instead of nanowires were grown as shown in **Figure 12**. **Figure 12(a)** and **(b)** shows respectively FESEM images of the surface and the cross section of a film deposited on a floating silicon substrate. **Figure 12(c)** and **(d)** shows those deposited on a grounded substrate. The deposition condition was the same as that of **Figure 11** except the gas flow rate of N_2. The film on the grounded substrate in **Figure 12(c)** and **(d)** was much more porous than that on the float-

http://dx.doi.org/10.5772/63926

ing substrate in **Figure 12(a)** and **(b)**. Therefore, quite different microstructures are evolved between the floating and grounded substrates, indicating that the dense film in **Figure 12(a)** and **(b)** resulted from the electrostatic interaction between the CNPs and the growing surface. The film thicknesses of **Figure 12(b)** and **(d)** were respectively ~220 and ~190 nm, indicating that the growth rate of the film on the floating substrate was higher than that on the grounded substrate. Besides, the film in **Figure 12(b)** is much denser than that in **Figure 12(d)**. Therefore, the mass increase on the floating substrate in **Figure 12(b)** is much higher than that on the grounded substrate in **Figure 12(d)**. This study also indicates that the deposition behavior of charged silicon nanoparticles differs dramatically between floating and grounded substrates due to the difference in the accumulation of charge between floating and grounded substrates. These results imply that charge plays a critical role in the evolution of dense films and smooth nanowires.

4.2. Comparison of deposition behavior between conducting and non-conducting surfaces

The concept of non-classical crystallization during PECVD was suggested by Cabarrocas et al. [23, 24, 70]. They reported that silicon nanoparticles formed in the gas phase during the PECVD process are incorporated into a polymorphous structure. They also suggested that high-quality films can be deposited at a high growth rate by incorporating those nanoparticles. In order to confirm whether nanoparticles, which are generated in the gas phase, should be charged or not, Cabarrocas et al. [70] examined the deposition behavior on 5×5 cm^2 glass substrates partially coated with Cr. They also compared the deposition behavior between the glass substrates with and without hydrogen plasma pretreatment as shown in **Figure 13**.

In the case of the glass substrate without any plasma treatment, no film was deposited on the uncoated part as shown in the right of **Figure 13**. In both cases of left and right in **Figure 13**, film deposition took place only on the Cr-coated part, which is a kind of selective deposition. On the other hand, for the glass substrate exposed to hydrogen plasma, the entire surface of the substrate was deposited as shown in the left of **Figure 13**. These results strongly support their hypothesis that the building blocks of the deposition are charged.

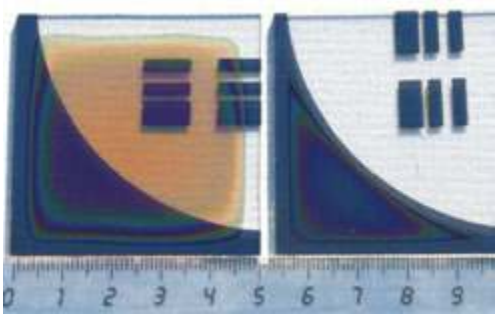

Figure 13. Image of two deposition behavior on partly Cr-coated glass substrates with a hydrogen plasma pretreatment (left) and without plasma pretreatment (right). Reprinted with permission from [70]. Copyright 2008 Elsevier.

4.3. Effect of flow rate on the deposition behavior in the silicon CVD process

The effect of various parameters in the CVD process should be newly understood based on the new paradigm of non-classical crystallization by CNPs. In this section, the effect of a carrier gas flow rate on the deposition behavior will be examined. Youn et al. [71] varied the flow rate of nitrogen carrier gas during atmospheric pressure silicon CVD and observed the microstructure evolution of films or nanostructures as shown in **Figure 14**.

Figure 14(a)–(d) shows the FESEM images of the surface microstructure of films or nanostructures synthesized on a quartz substrate respectively at nitrogen flow rates of 300, 500, 700, and 1000 sccm. At 300 sccm (**Figure 14(a)**), nanowires were grown with nanoparticles attached to nanowires. At 500 sccm (**Figure 14(b)**), nanowires were grown extensively. At 700 sccm (**Figure 14(c)**), a film was grown at first and then a porous structure evolved on the initial film. At 1000 sccm (**Figure 14(d)**), a relatively dense film was grown.

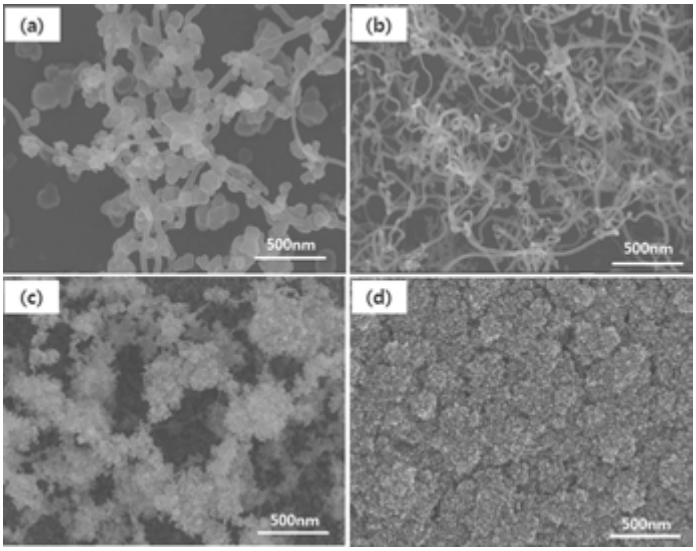

Figure 14. FESEM images of silicon films and nanostructures. The various microstructures of silicon evolved on a quartz substrate at N_2 gas flow rates of (a) 300, (b) 500, (c) 700, and (d) 1000 sccm. Reprinted with permission from [71]. Copyright 2013 Elsevier.

These results indicate that the carrier gas flow rate greatly affects microstructure evolution. To examine the effect of the carrier gas flow rate on the generation of CNPs in the gas phase, in-situ measurements of the CNPs were made using a DMA-FCE (Faraday cup electrometer) system under the same conditions as those of **Figure 14**. **Figure 15(a)** and **(b)** shows respectively the size distribution of negatively and positively charged silicon nanoparticles at various carrier flow rates. As the flow rate decreased, the number concentration of negative and positive CNPs decreased but the peak of the size distribution increased. In the case of positive CNPs in **Figure 15(b)**, the number concentration of ~40 nm nanoparticles at 1000 sccm of N_2

http://dx.doi.org/10.5772/63926

is roughly 100 times larger than that at 500 sccm. When the carrier flow rate is lower than 500 sccm, nanoparticles smaller than 20 nm were not detected.

Figure 14 shows that the amount of deposition on the substrate in terms of mass is decreased with decreasing flow rate of the carrier gas. This aspect would be related with **Figure 15**, which shows that the number concentration of CNPs generated in the gas phase is decreased with decreasing flow rate. The study indicated that the microstructure evolution of films, nanowires, and nanoparticles is closely related to the number concentration of CNPs, which is affected by the carrier gas flow rate.

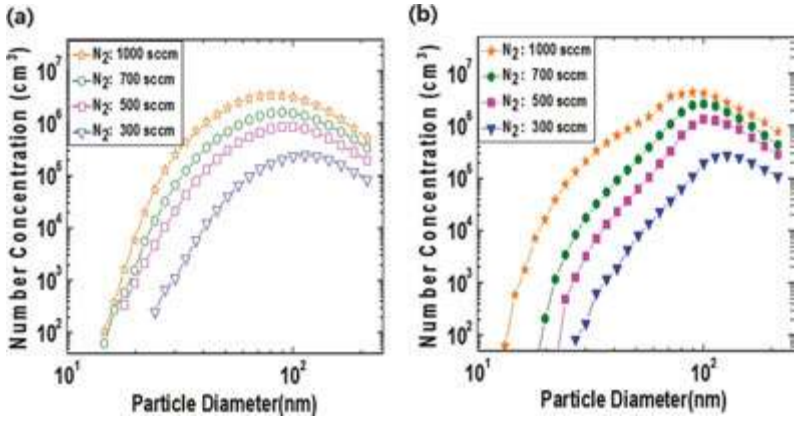

Figure 15. The number concentration and size distribution of (a) negative and (b) positive CNPs at various N_2 gas flow rates of 300, 500, 700, and 1000 sccm. Reprinted with permission from [71]. Copyright 2013 Elsevier.

Then why do the amount of the deposition and the number concentration of CNPs decrease with decreasing flow rate? What is found is that silicon tends to deposit on the tube wall near the inlet in the temperature zone of 600–800 °C, which is higher than the decomposition temperature of SiH_4. It is further observed that the amount of silicon deposited on the tube wall increases with decreasing flow rate of the carrier gas. This means that the loss of silicon on the tube wall before the hot zone at the center of the reactor is responsible for the decrease in amount of deposit on the substrate and the number concentration of charged gas-phase nuclei with decreasing flow rate.

With decreasing flow rate of the carrier gas, the mean residence time of the gas would be increased in the reactor although the total amount was decreased due to the loss on the tube wall before the hot zone. The slight increase of the particle diameter of maximum size with decreasing flow rate as shown in **Figure 15** might come from the increased mean residence time. Therefore, the deposition on the tube wall depends on the flow rate, which can be understood by the drag force imposed on CNPs by impinging molecules. When nanoparticles are the building blocks of crystal growth, the drag force should be considered in understanding the deposition behavior. Even under the condition where CNPs are generated in abundance, they might not be able to deposit because of the drag force if the flow rate in the direction

parallel to the substrate is high enough. In relation to the drag force, Park et al. [72] studied the effect of the bias on the deposition behavior of ZnO nanostructures as follows.

4.4. Effect of bias on the deposition behavior of ZnO nanostructures in the CVD process

It was often found that even under the condition where CNPs are generated abundantly in the gas phase, the deposition of films or nanostructures does not occur on the substrate in specific locations of the CVD. Since non-deposition of films or nanostructures under the generation condition of CNPs would be caused by the drag force, the drag force is an important factor to be considered in the deposition of CNPs. Even when the deposition by CNPs was inhibited by the drag force, the existence of CNPs may be revealed by applying the electrical bias to the substrate. If the bias overcomes the drag force, CNPs that could not deposit on a substrate should be attracted toward the substrate and the deposition occurs. Park et al. [72] confirmed this possibility by examining the bias effect on the deposition behavior in the CVD reactor where charged ZnO nanoparticles are generated in the gas phase.

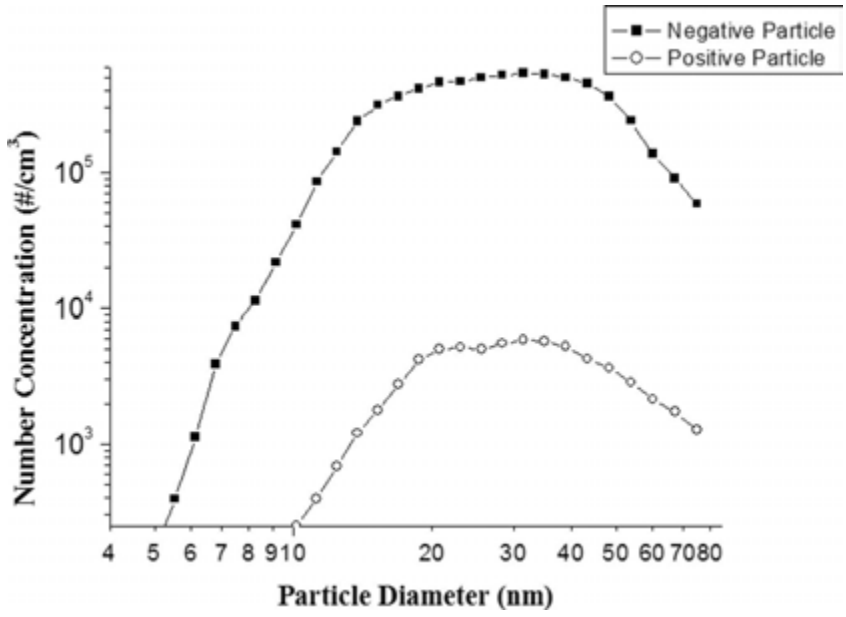

Figure 16. Size distribution of charged ZnO nanoparticles that were generated in the gas phase during the synthesis of ZnO nanostructures. Reprinted with permission from [72]. Copyright 2015 Elsevier.

Figure 16 shows the size distribution of ZnO CNPs measured by the DMA-FCE system. This result indicates that the number of CNPs in gas phase of the CVD system is large enough. However, they do not land on the substrate placed in 450 °C zone, which is rather near the outlet, being away from the center of the reactor. Then, why don't they land on the substrate placed in 450 °C zone as shown in **Figure 17(a)**?

One possible answer would be the drag force. The drag force is influenced by the relative velocity of particles in the medium [73]. Considering gas flow dynamics in the reactor, the hot gas that comes from the heated reactor zone would move upward over the colder gas in the unheated zone because of the density difference arising from the temperature gradient. This gas stream would exert a drag force on the nanoparticles that are generated in the hot zone so that they would move upward over the gas of 450 °C zone. To test this possibility, the electric bias was applied to the substrate holder.

The result is shown in **Figure 17**. As previously reported, charged tetrapod ZnOs as well as charged ZnO nanoparticles are generated in the gas phase during the synthesis of ZnO nanostructures [74]. This fact helps us understand the results of **Figure 17**. When +100 V was applied to the substrate holder of stainless steel, ZnO nanoparticles of ~10 nm were deposited not in a little amount on the silicon substrate as shown in **Figure 17(b)**. When the bias was increased to +300 V, slightly larger ZnO nanoparticles of ~40 nm were deposited in an appreciable amount as shown in **Figure 17(c)**. When the bias was increased even further to +600 V, tetrapod ZnOs were deposited as shown in **Figure 17(d)**. SEM observations at higher magnification revealed that tetrapod-ZnOs were deposited together with smaller ZnO nanoparticles. **Figure 17(b)–(d)** shows that as the bias voltage increased, the size of particles that could be deposited increased. This bias experiment shows that the charged ZnO nanoparticles are under the influence of the drag force and explains why CNPs measured in **Figure 16** did not land on the substrate in **Figure 17(a)**. A drag force exerting on particles by the gas flow is expressed as

$$F_D = 1/2 C_D A \rho v^2 \tag{7}$$

where F_D = drag force, C_D = drag coefficient, A = cross sectional area perpendicular to the flow, ρ = density of the medium, v = velocity of the body relative to the medium. This equation reveals that particles with a large area have a larger drag force and thereby larger resistance to move toward the substrate than those with a smaller area. Therefore, in order to deposit large particles, a high bias voltage is needed because of the high drag force arising from the upward gas stream caused by the temperature gradient. Non-deposition in **Figure 17(a)** can be understood on the basis of the drag force: under zero bias voltage, ZnO particles generated in the gas phase would just flow out with the carrier gas because the drag force inhibited the particles from moving toward the substrate. Also, under the bias of +100 V in **Figure 17(b)**, small particles of ~10 nm could be deposited, but large particles would flow out with the carrier gas. Because the drag force for small charged particles is weak, only a small electric force is needed to overcome the drag force of the small particles, which results in the deposition of small charged particles on the substrate. Under the bias of +300 V in **Figure 17(c)**, slightly larger particles of ~40 nm could be deposited with much larger particles being flowed out with the carrier gas. Under the bias of +600 V in **Figure 17(d)**, however, even larger tetrapod particles with a leg length of ~600 nm could be deposited on a substrate, indicating that the electric force is high enough to overcome the drag force. The gravity of these nanosized particles appeared to be much smaller than the electric force and could be ignored. These

results indicated that the drag force becomes an important factor in deposition when nanoparticles are formed in the gas phase.

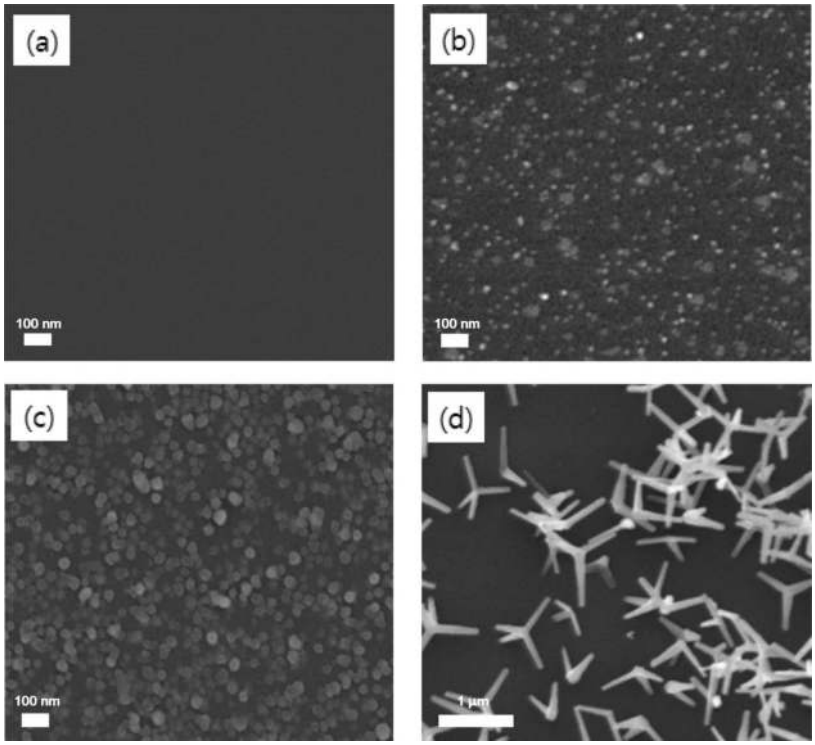

Figure 17. Deposition behavior of charged ZnO particles under the positive biases of (a) 0 V, (b) +100 V, (c) +300 V, and (d) +600 V. Reprinted with permission from [72]. Copyright 2015 Elsevier.

4.5. Effect of alternating bias on the deposition behavior of silicon in the CVD process

In the previous section, it was shown that even under the condition where CNPs are generated in abundance, they might not contribute to deposition because of the drag force. In this case, applying the DC bias would be effective to deposit those CNPs in the gas phase when CNPs are somewhat conducting as shown in **Figure 17**. When the CNPs are insulating, however, the positive bias would attract the negative CNPs and then negative charge would build up on the surface. This built-up charge would diminish the effect of the positive bias and then the positive bias would not be pronounced any more. In this case, the alternating bias would be effective because it prevents charge build up on the growing surface.

Youn at el. [75] studied the effect of alternating bias in silicon deposition on stainless substrate holder during thermal CVD. The bias frequency and voltage were varied. **Figure 18** shows the FESEM images of the surface morphology of silicon films deposited on the quartz substrates

http://dx.doi.org/10.5772/63926

for 2 hours at reactor temperature of 900°C with gas flow rates of 5 sccm 10% SiH_4–90% He, 50 sccm H_2, and 1000 sccm N_2. **Figure 18(a)–(d)** is for the zero bias and the bias voltage of ±100 V at frequencies of 0.2, 0.5, and 5 Hz, respectively. **Figure 18(a)** shows the microstructure of the film which was deposited under the condition of the zero bias. The film has some roughness on the surface. This surface microstructure of the film is similar to that of films deposited by PECVD [76] and HWCVD [66]. **Figure 18(b)**, the microstructure of film which was deposited at a frequency of 0.2 Hz, shows the surface is covered by flake-like structures. At 0.5 Hz, the surface became smoother than that of 0.2 Hz and a flake-like structure disappeared as shown in **Figure 18(c)**. The surface of film which was deposited at 5 Hz had a very porous structure as shown in **Figure 18(d)**.

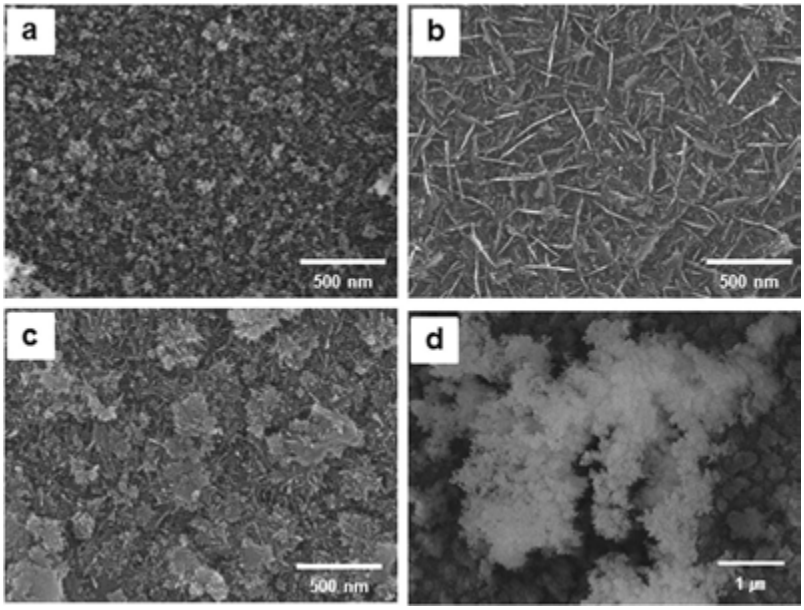

Figure 18. FESEM image of silicon deposited during 2 hour on a quartz substrate at (a) zero bias, (b) AC bias voltage of ±100 V with frequencies 0.2 Hz, (c) AC bias voltage of ±100 V with frequencies 0.5 Hz, and (d) AC bias voltage of ±100 V with frequencies 5 Hz. Reprinted with permission from [75]. Copyright 2012 Elsevier.

The effect of the bias voltage was also examined. The bias was applied to the stainless substrate holder at the biases of ±50 V, ±100 V, ±150 V, and ±200 V with a frequency of 1 Hz. **Figure 19** shows the FESEM images of the surface morphology of silicon films deposited under the same processing condition as that of **Figure 18**. Under the bias of ±50 V, the film microstructure tended to have a flake-like structure as shown in **Figure 19(a)**. When the bias was increased to ±100 V, the microstructure tended to have round nodules as shown in **Figure 19(b)**. When the bias was increased to ±150 V, the microstructure became porous as shown in **Figure 19(c)**. On applying ±200 V bias, the nanoparticles of ~100 nm were aggregated as a chain-like structure with their surface covered with numerous nano-rods as shown in **Figure 19(d)**. The nanopar-

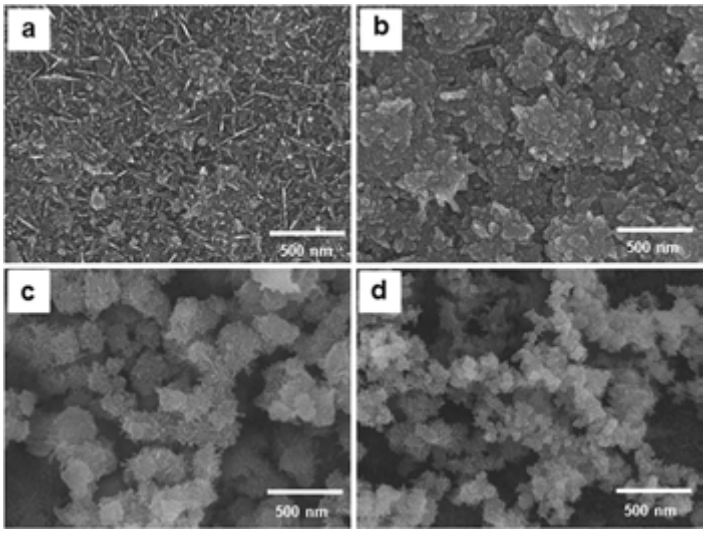

Figure 19. FESEM images of silicon films deposited on a quartz substrate at AC bias voltages of (a) ±50 V, (b) ±100 V, (c) ±150 V, and (d) ±200 V with the frequency of 1 Hz applied to the substrate holder. Reprinted with permission from [75]. Copyright 2012 Elsevier.

ticles of ~50 nm were deposited on the surface, being smaller than those deposited at ±150 V. The microstructure deposited at ±200 V was much more porous than that deposited at ±150 V.

These results imply that controlling the AC bias frequency or the magnitude of bias voltages may produce various microstructures. Besides, the AC bias technique can provide a promising method to produce highly porous microstructures, which are favorable for low dielectric materials.

Various microstructures can be synthesized by changing the bias frequency and the magnitude of bias voltages during deposition. By this technique, films of a layered structure with each layer of different microstructures can be synthesized. For example, the first layer is made dense, the second layer being porous, and the third layer being dense again. These results show clearly that the bias, either AC or DC, can be a new processing parameter in the CVD process where CNPs are generated.

4.6. Effect of size of CNPs on CVD process

The size of CNPs is also a critical factor in thin film growth by CVD. Therefore, information about the size distribution of CNPs is important in controlling the microstructure evolution of films. The size of nanoparticles increases normally as the concentration of reactant source gases increases. **Figure 20** shows the measured mass distributions of negative CNPs for four different methane concentrations during HWCVD [60]. During the mass distribution measurements, diamonds were deposited in situ on a Mo substrate placed near the orifice

http://dx.doi.org/10.5772/63926

with a substrate temperature of 750 °C. The diamond films deposited at 1% and 1.5% CH_4, where nanoparticles of 200–300 carbon atoms were dominant as shown in **Figure 20**, showed good crystalline quality as shown in **Figure 21(a)**. For methane concentrations of 3% and 5%, where the nanoparticles in the gas phase contained more than 1000 carbon atoms and the size distribution became much broader in **Figure 20**, ball-like diamonds were deposited as shown in **Figure 21(b)**. This structure is often called a cauliflower structure because it looks similar to the vegetable cauliflower.

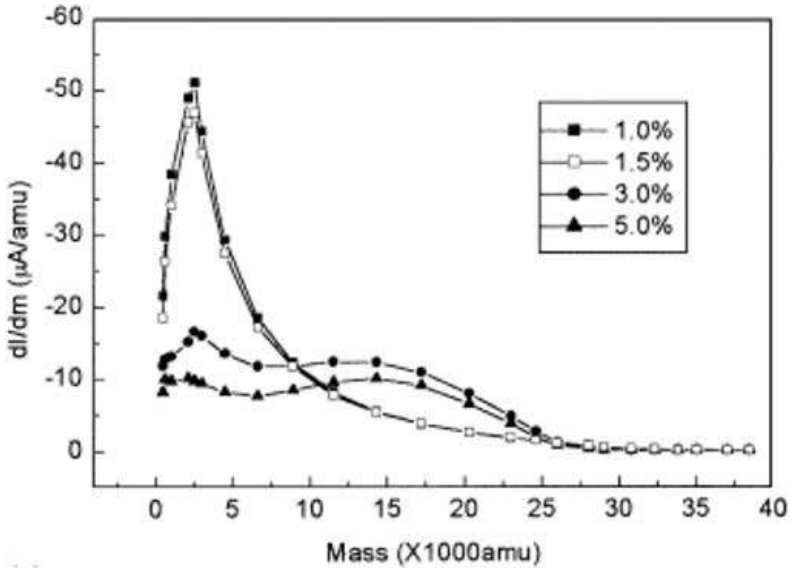

Figure 20. Measured mass distributions of negatively charged carbon clusters extracted from the hot filament reactor using gas mixtures of 1% CH_4-99% H_2, 1.5% CH_4-98.5% H_2, 3% CH_4-97% H_2, and 5% CH_4-95% H_2. Reprinted with permission from [60]. Copyright 2001 Elsevier.

To explain such an effect of size of CNPs on the microstructure evolution, weakening of bond strength by charge should be considered. In a soft charging condition such as thermal and hot wire CVD, which is in contrast with the hard charging condition in plasma CVD, most nanoparticles are expected to be singly charged. In this case, the charge effect on weakening of the bond strength would be diminished as the size increases. In other words, the smaller CNPs would be more liquid-like than the larger ones. Therefore, large CNPs generated under the high methane concentration in **Figure 20** would be less liquid-like so that CNPs frequently fail to undergo epitaxial recrystallization, producing ball-like or cauliflower diamond structures as shown in **Figure 21(b)**. On the other hand, small CNPs generated under the low methane concentration in **Figure 20** would be more liquid-like so that CNPs mostly undergo epitaxial recrystallization, producing high-quality diamonds with well-defined facets as shown in **Figure 21(a)**.

To confirm the effect of nanoparticle size on the deposition behavior, Yoshida and his colleagues [77–81] made extensive studies on the epitaxial growth of films with a building block of nanoparticles by the method called thermal plasma flash evaporation. They could deposit high-quality epitaxial $YBa_2Cu_3O_{7-x}$ films with a growth rate as high as 16 nm/s by this technique. They also could estimate the size of the nanoparticles to be about 0.3–10 nm using a microtrench fabricated on a Si wafer [79]. They observed that small 1–2 nm nanoparticles made epitaxial spiral growth, medium size 3 nm nanoparticles produced epitaxial 2-dimensional particles, and large nanoparticles over 3 nm produced non-epitaxial island grains by scanning tunneling microscopy (STM) [80].

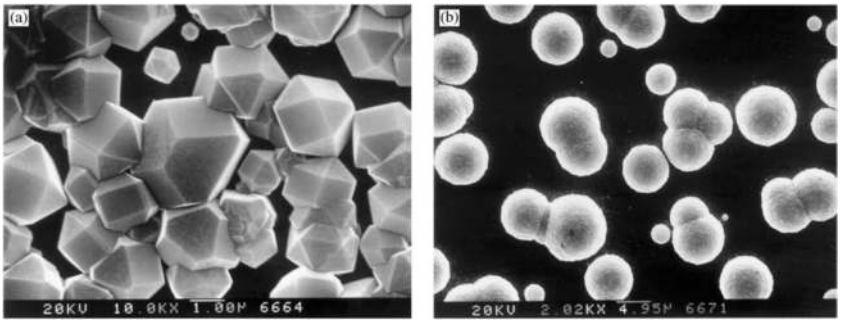

Figure 21. SEM images of diamond films deposited *in situ* during the measurement of the mass distribution of CNPs at 2100°C wire temperature and 800 Pa reactor pressure: (a) 1% CH_4-99%nH_2, (b) 3% CH_4-97%H_2. Reprinted with permission from [60]. Copyright 2001 Elsevier.

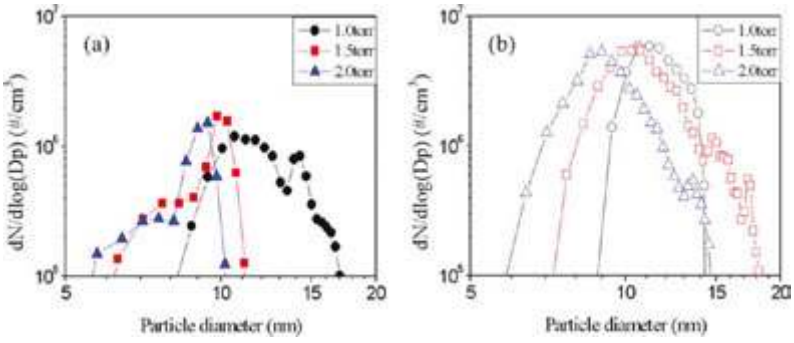

Figure 22. Size distribution of positively (a) and negatively (b) charged silicon nanoparticles measured by PBMS at a wire temperature of 1800°C with various process pressures during HWCVD. Reprinted with permission from [82]. Copyright 2014 Elsevier.

The reactor pressure also affects the size of CNPs. Yoo et al. [82] investigated the size distribution of CNPs generated in the gas phase during deposition of Si films by HWCVD through particle beam mass spectrometry (PBMS).

http://dx.doi.org/10.5772/63926

Figure 22 shows the size distribution of CNPs generated in the gas phase measured by PBMS in the HWCVD process with a 4% SiH_4–96% H_2 gas mixture and a wire temperature of 1800°C at 1.0, 1.5, and 2.0 Torr. The peak of the number concentration occurs at 9–12 nm at which the number concentrations of both positive and negative CNPs are 10^6–10^7 /cm^3. These nanoparticles were observed by TEM after being captured from the gas phase on a TEM grid membrane. As the pressure is increased from 0.3 to 2 Torr, not only the size and the number of captured nanoparticles are decreased, but also the rate of deposition is increased. An increase in the distance at which nanoparticles were captured from the hot wires under 1.5 Torr also reduced the size and number of nanoparticles.

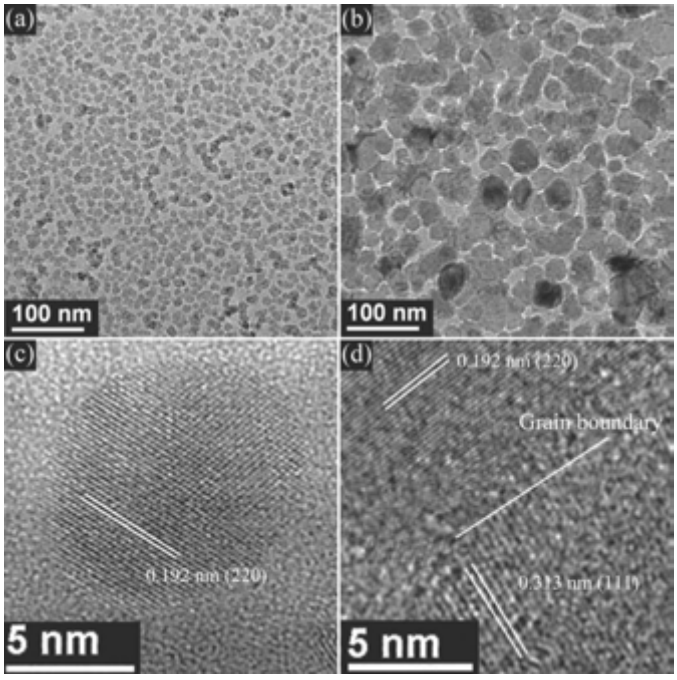

Figure 23. TEM images of initial silicon nanoparticles deposited for 20 sec after delay times of (a) 0 min and (b) 5 min and (c) and (d) showing respectively the HR images of (a) and (b). Reprinted with permission from [83]. Copyright 2012 Elsevier.

Chung et al. [83] show that the size of silicon nanoparticles generated in the gas phase during HWCVD tended to increase with increasing processing time and the size tended to be saturated above 15 min. This means that the steady state in terms of the size of CNPs is not reached in the reactor until 15 min. Therefore, in the initial stage of deposition before 15 min, small CNPs would deposit whereas in the later stage after 15 min, large CNPs would deposit. Therefore, if beginning of the deposition is delayed using the shutter above the substrate, the size of CNPs to be deposited can be controlled. Based on this observation, Chung et al. [83] used the concept of the delay time in deposition to control the microstructure. How the size of CNPs changes

with the delay time can be examined by capturing CNPs on a TEM grid membrane with different delay times.

For example, **Figure 23(a)** and **(b)** shows the silicon nanoparticles captured on a Cu TEM grid membrane for 20 sec with delay times of 0 and 5 min, respectively. **Figure 23(c)** and **(d)** is the magnified view showing the lattice image of **Figure 23(a)** and **(b)**, respectively. The sizes of crystalline silicon nanoparticles in **Figure 23(a)** and **(b)** are ~10 and ~28 nm, respectively. The lattice image in **Figure 23(c)** shows a (220) plane, and that of **Figure 23(d)** consists of (220) and (111) planes, indicating that the silicon particle is a bicrystal.

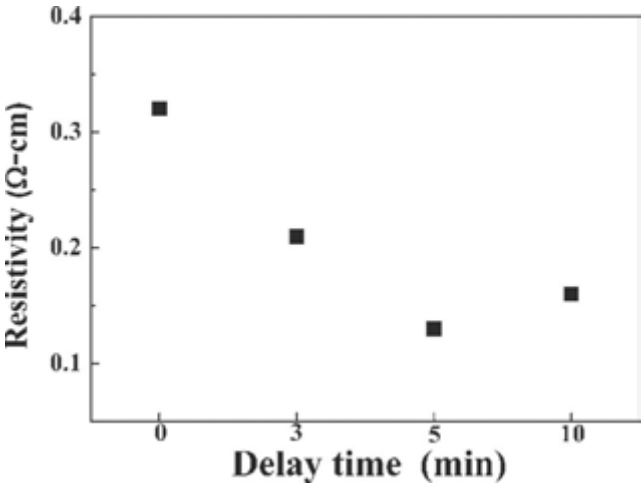

Figure 24. Resistivity of silicon films with the initial silicon layer deposited for 300 sec after delay times of 0, 3, 5, and 10 min. Reprinted with permission from [83]. Copyright 2012 Elsevier.

In order to study the effect of a different initial layer, the initial layer was deposited on the glass substrate for 20 sec after delay times of 0, 3, 5, and 10 min using the shutter. Then, these four samples were further deposited for 300 sec under the same processing conditions as that of **Figure 23**, and the resistivity of the deposited silicon films was measured. **Figure 24** shows how the resistivity of the silicon films varies with delays times. The thickness of all the films was ~170 nm. The resistivity of a silicon film deposited without a delay time (or a delay time of 0 min) is 0.32 Ω-cm. It should be noted that such low resistivity is due to HCl addition; silicon films deposited without HCl by PECVD or HWCVD have resistivity typically in the range of 5–50 Ω-cm [84, 85]. The resistivities of the silicon films prepared with delay times of 3, 5, and 10 min are 0.21, 0.13, and 0.16 Ω-cm, respectively. The resistivity tended to be saturated after a delay time of 5 min. Silicon films with a delay time show consistently lower resistivity than those without a delay time. The lowest resistivity of 0.13 Ω -cm of the film with a delay time of 5 min is 2.4 times lower than that without a delay time.

This resistivity change with delay times can be understood considering the property of CNPs. Without a delay time, the size of CNPs would be minimal and more liquid-like. These liquid-

like CNPs, which would be accommodated to the substrate of an amorphous glass structure, would change to an amorphous structure, resulting in high resistivity. In contrast, with a delay time of 10 min, the size of CNPs would be maximal and less liquid-like. These CNPs would retain their crystalline silicon structure instead of changing to an amorphous structure, resulting in low resistivity.

4.7. Low-temperature deposition of crystalline silicon

There is a strong need for the low temperature synthesis of crystalline silicon films for electronics such as displays and solar cells [86–89]. The most popular method to synthesize microcrystalline films is to deposit amorphous phase silicon on a glass substrate than to crystallize it by excimer laser, thermal annealing, or metal-induced crystallization [90–92]. Since these methods increase the production cost, it is necessary to deposit the crystalline silicon film directly on a glass substrate.

From the view point of classical crystallization, silicon diffusivity below 600 °C is so low that amorphous silicon is expected on a glass substrate below 600 °C. Direct deposition of crystalline silicon at temperatures below 600 °C is not possible. Nonetheless, the direct deposition of microcrystalline silicon films on a glass substrate below 400 °C has been reported using HWCVD system [93–95] or PECVD system [96]. These results cannot be approached by the concept of classical crystallization. However, this low temperature deposition of crystalline silicon can be explained by non-classical crystallization. If crystalline silicon nanoparticles were formed in the gas phase in a high-temperature region near the hot wire and then incorporated into the films at low temperature, crystalline silicon could be deposited on a substrate at temperature below 600 °C.

If this explanation is correct, crystalline silicon nanoparticles should exist in the gas phase, which can be confirmed by capturing them on a TEM grid membrane. For this experimental confirmation, Lee et al. [84] designed the HWCVD, which consists of three chambers by two stage orifices. Each chamber was maintained in different pressures by two-stage differential pumping. The first chamber is the HWCVD reactor with the working pressure maintained at 27 Pa under a flowing gas mixture of SiH_4 and H_2, and the working pressure of the third chamber being maintained at 1.3×10^{-3} Pa during the process. The CNPs were generated in the first chamber and extracted through the first and the second orifices into the third chamber.

These CNPs were captured on the TEM grid located in the third chamber at room temperature. The wire temperature was 1560°C and the concentration of SiH_4 in the gas mixture of SiH_4-H_2 was varied as 20%, 15%, 10%, and 5%. The TEM image of the crystalline silicon CNPs captured on the TEM grid membrane is shown in **Figure 25** [84]. The CNPs which were captured on the TEM grid membrane had the crystallinity and the lattice fringes of CNPs were clearly revealed. The size of the crystalline nanoparticles decreased with decreasing SiH_4 concentration with 7–8 nm for 20% SiH_4 (**Figure 25(a)**), 6–7 nm for 15% SiH_4 (**Figure 25(b)**), 5–6 nm for 10% SiH_4 (**Figure 25(c)**), and 4–5 nm for 5% SiH_4 (**Figure 25(d)**).

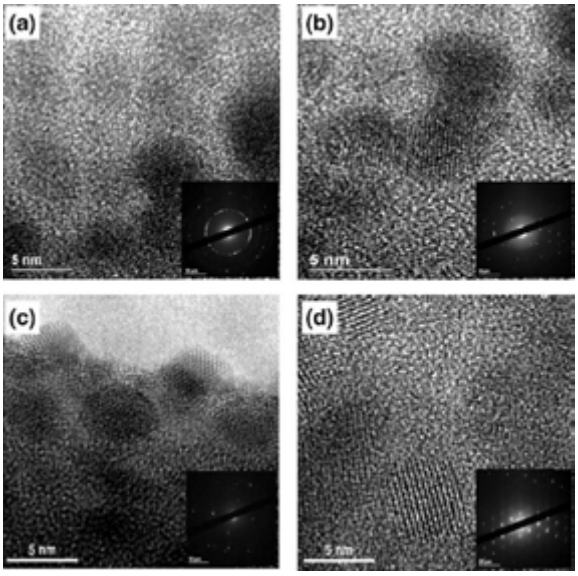

Figure 25. TEM images of silicon nanoparticles which were captured on the amorphous carbon membrane at room temperature by HWCVD with (a) 20%, (b) 15%, (c) 10% and (d) 5% flow rate of SiH_4 at a wire temperature of 1560°C. Reprinted with permission from [84]. Copyright 2008 Elsevier.

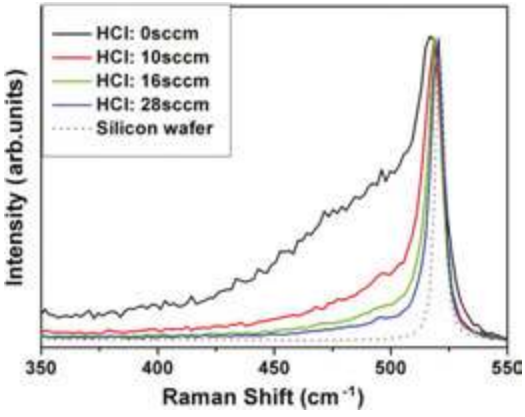

Figure 26. Raman spectra of the silicon films deposited at various HCl flow rates. The dotted line is for a single crystal silicon wafer as a reference. Reprinted with permission from [97]. Copyright 2009 Elsevier.

Classical crystallization cannot explain such formation of crystalline silicon nanoparticles at room temperature because the atomic diffusion rate is negligible. **Figure 25** strongly indicates that CNPs were formed in the gas phase of the first chamber during HWCVD and landed on the TEM grid in the third chamber.

http://dx.doi.org/10.5772/63926

There is an appreciable amount of amorphous silicon in the TEM images. This amorphous phase is expected to have been formed in the low-temperature region far from the hot wire. Therefore, to minimize the amorphous phase, low-temperature precipitation or nucleation of silicon should be inhibited. To inhibit the precipitation of silicon at low temperature, Chung et al. [97, 98] suggested HCl addition to SiH_4. Further, they confirmed that the crystallinity of silicon increased with increasing HCl addition as revealed in the Raman spectra of **Figure 26**. Since the Si-Cl-H system has retrograde solubility [99], if HCl is added to the Si-H system, the solubility of silicon in the gas phase increases with decreasing temperature, which means the equilibrium amount of silicon decreases with decreasing temperature.

This means that when gas-phase nucleation occurs, the driving force near the substrate temperature becomes for etching as in the case of the C-H system for diamond CVD. Therefore, HCl addition inhibits the precipitation of amorphous silicon at low temperature. Then, the crystalline silicon nanoparticles, which are precipitated at high temperature, will exclusively contribute to deposition without additional precipitation of amorphous silicon at low temperature, improving the crystallinity of the film.

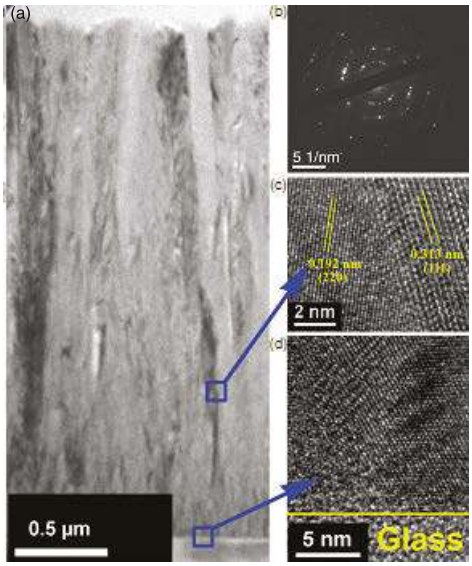

Figure 27. TEM images of the *n*-type crystalline silicon film with HCl (a) a bright-field image, and (b) image of the selective area diffraction pattern with (c) and (d) being high-resolution images on the regions indicated in (a). Reprinted with permission from [98]. Copyright 2011 Elsevier.

It is known that an amorphous silicon incubation layer, which is as thick as hundreds of nanometers, is formed on the glass substrate before crystalline silicon starts to form when the low temperature deposition of crystalline silicon is done by HWCVD or PECVD. The formation of such an amorphous incubation layer is a serious problem for thin-film transistor (TFT) applications because the thickness of the TFT should be typically less than ~200 nm.

Chung et al. [97, 98] could successfully minimize the formation of amorphous incubation layer by adding HCl as shown in **Figure 27**.

Figure 27 shows the cross section HRTEM images of the crystalline silicon film deposited at the flow rate ratios of [HCl]/[SiH_4] = 7.5 and [PH_3]/[SiH_4]=0.028. The whole deposition area of **Figure 27(a)** consists of crystalline silicon. More specifically, the high-resolution image at the middle of the film in **Figure 27(c)** reveals that the grain boundary is free from any amorphous phase between the two grains showing (111) and (220) planes. This aspect is highly in contrast with the previous result, where HCl was not added, that the crystalline silicon nanoparticles were embedded in the amorphous silicon phase. **Figure 27** showed that the amorphous incubation layer could be reduced markedly or almost removed by HCl addition. This is an example showing how new understanding of thin film growth by non-classical crystallization can be applied.

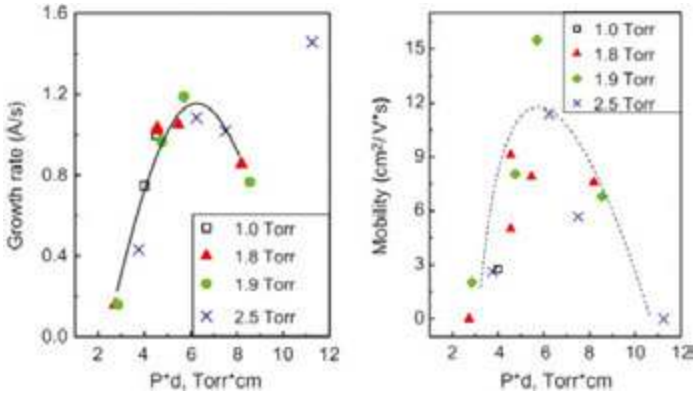

Figure 28. Growth rate and electron mobility from time-resolved microwave conductivity measurements of the total pressure and the distance of inter-electrode. Reprinted with permission from [70]. Copyright 2008 Elsevier.

As to the possibility of incorporation of particles generated in the gas phase during PECVD, Cabarrocas et al. [23, 24, 70, 96] suggested that the nanoparticles generated in the gas phase can be incorporated into films. Cabarrocas et al. [70] reported that the incorporation of crystalline nuclei generated in the gas phase increased the film deposition rate and electron mobility of films. This result is shown in **Figure 28**, where the x-axis is the product of the total pressure and inter-electrode distance. Both film growth rate and electron mobility are maximum when the process pressure is ~ 6 Torr.

They could deposit fully crystallized films, consisting of 68% small grain materials and 28% monocrystalline silicon with a 4% fraction of voids at substrate temperature of 200 °C, RF power at 20 W and gas flow rates at 1, 5, and 36 sccm respectively for SiF_4, H_2, and Ar. Considering the substrate temperature of 200 °C, the deposition of microcrystalline films also cannot be explained by classical crystallization. Therefore, the high crystallinity of films also would be attributed to the self-assembly of CNPs formed in the gas phase.

http://dx.doi.org/10.5772/63926

However, the temperature of the plasma is too low to form the crystalline silicon phase in the gas phase. This question would be explained by the role of charges produced in the plasma CVD, by which not only the kinetics of the precursor decomposition is enhanced, but also the deposition of crystalline films is made possible at such low temperatures. All these enhanced kinetics can be explained if the charge weakens the bond strength of molecules and nanoparticles.

5. Conclusion

Non-classical crystallization, where the growth units of deposition in CVD process are CNPs, was revealed by the rigorous thermodynamic analysis of the paradoxical experimental observation of simultaneous diamond deposition and graphite etching. This mechanism was further supported by the puzzling phenomenon of diamond deposition on a silicon substrate and porous skeletal graphitic soot deposition on an iron substrate. This new paradigm of crystal growth was also experimentally confirmed in many CVD processes, which means that non-classical crystallization is a general growth mechanism of thin films and nanostructures in CVD processes. Lots of fundamental and application studies should be made in this new paradigm of crystal growth.

Acknowledgements

This work was supported by the Global Frontier R&D Program (2013-073298) on Center for Hybrid Interface Materials (HIM) funded by the Ministry of Science, ICT & Future Planning and National Research Foundation of Korea(NRF) grant funded by the Ministry of Science, ICT & Future Planning(MSIP) (NO. NRF-2015R1A5A1037627).

Author details

Jae-soo Jung[1] and Nong-moon Hwang[2*]

*Address all correspondence to: nmhwang@snu.ac.kr

1 Department of Material Science and Engineering, Seoul National University, Gwanak-gu, Seoul, Republic of Korea

2 Department of Material Science and Engineering, Seoul National University and Research Institute of Advanced Materials (RIAM), Seoul National University, Gwanak-gu, Seoul, Republic of Korea

References

[1] Boufendi L, Plain A, Blondeau J P, Bouchoule A. Laure C Toogood M, Measurements of particle size kinetics from nanometer to micrometer scale in a low-pressure argon-silane radio-frequency discharge. Appl. Phys. Lett. 1992;60:169. DOI: 10.1063/1.106981

[2] Howling A A, Sansonnens L, Dorier J L, Hollenstein C. Negative hydrogenated silicon ion clusters as particle precursors in RF silane plasma deposition experiments J. Phys. D: Appl. Phys. 1993;26:1003. DOI: 10.1088/0022-3727/26/6/019

[3] Veprek S, Ambacher O, Rieger W, Schopper K, Veprek-Heijman M G J. Clusters in a silane glow discharge: mechanism of their formation and how to avoid them. Mater. Res. Soc. Symp. Proc. 1993;297:13. DOI: 10.1557/PROC-297-13

[4] Garscadden A, Ganguly B N, Haaland P D, Williams J. Overview of growth and behaviour of clusters and particles in plasmas. Plasma Sources Sci. Technol. 1994;3:239. DOI: 10.1088/0963-0252/3/3/001

[5] Stoffels E, Stoffels W W, Kroesen G M W, Hoog F J D. Dust formation and charging in an Ar/SiH_4 radio-frequency discharge. J. Vac. Sci. Technol. A. 1996;14:556. DOI: 10.1116/1.580144

[6] Hwang N M, Yoon D Y. Thermodynamic approach to the paradox of diamond formation with simultaneous graphite etching in the low pressure synthesis of diamond. J. Cryst. Growth. 1996;160:98. DOI: 10.1016/0022-0248(95)00549-8

[7] Hwang N M, Hahn J H, Yoon D Y. Charged cluster model in the low pressure synthesis of diamond. J. Cryst. Growth. 1996;162:55. DOI: 10.1016/0022-0248(95)00943-4

[8] Hwang N M, Hahn J H, Yoon D Y. Chemical potential of carbon in the low pressure synthesis of diamond. J. Cryst. Growth. 1996;160:87. DOI: 10.1016/0022-0248(95)00548-X

[9] Hwang N M, Kim D Y. Charged clusters in thin film growth. Int. Mater. Rev. 2004;49:171. DOI: 10.1179/095066004225021891

[10] Hwang N M, Lee D K. Charged nanoparticles in thin film and nanostructure growth by chemical vapour deposition. J. Phys. D: Appl. Phys. 2010;43:483001. Review Paper. DOI: 10.1088/0022-3727/43/48/483001

[11] Jeon J D, Park C J, Kim D Y, Hwang N M. Experimental confirmation of charged carbon clusters in the hot filament diamond reactor. J. Cryst. Growth. 2001;213:79. DOI: 10.1016/S0022-0248(00)00358-4

[12] Ahn H S, Park H M, Kim D Y, Hwang N M. Observation of carbon clusters of a few nanometers in the oxyacetylene diamond CVD process. J. Cryst. Growth. 2002;234:399. DOI: 10.1016/S0022-0248(01)01748-1

[13] Jeon I D, Gueroudji L, Kim D Y, Hwang N M. Temperature dependence of the deposition behavior of yttria-stabilized zirconia CVD films: approach by charged cluster

model. J. Korean Ceram. Soc. 2001;38:218. DOI: http://www.dbpia.co.kr/Journal/ArticleDetail/NODE00737510

[14] Kim J Y, Kim D Y, Hwang N M. Spontaneous generation of negatively charged clusters and their deposition as crystalline films during hot-wire silicon chemical vapor deposition. Pure Appl. Chem. 2006;78:1715. DOI: 10.1351/pac200678091715

[15] Lee J I, Hwang N M. Generation of negative-charge carriers in the gas phase and their contribution to the growth of carbon nanotubes during hot-filament chemical vapor deposition. Carbon. 2008;46:1588. DOI: 10.1016/j.carbon.2008.07.006

[16] Kim C S, Chung Y B, Youn W K, Hwang N M. Generation of charged nanoparticles during the synthesis of carbon nanotubes by chemical vapor deposition. Carbon. 2009;47(10):2511–2518. DOI: 10.1016/j.carbon.2009.05.005

[17] Kim C S, Chung Y B, Youn W K, Hwang N M. Generation of charged nanoparticles during synthesis of ZnO nanowires by carbothermal reduction. Aerosol Sci. Technol. 2009;43(2):120–125. DOI: 10.1080/02786820802499068

[18] Kim C S, Kwak I J, Choi K J, Park J G, Hwang N M. Generation of charged nanoparticles during the synthesis of silicon nanowires by chemical vapor deposition. J. Phys. Chem. C. 2010;114:3390. DOI: 10.1021/jp910242a

[19] Bennema P, Gilmer G H. 1973 Crystal Growth: An Introduction, ed. P Hartman. Wiley; 2010. 1276 p. DOI: 10.1002/bbpc.19740781138

[20] van der Eerden J P. Handbook of Crystal Growth, vol. 1. In: A Fundamentals 'Thermodynamics and Kinetics'. Amsterdam: North-Holland. DOI: 10.1107/S010876739400512X

[21] McMurry P H. Investigation of particle generation during the low-pressure chemical vapor deposition of borophosphosilicate glass films. J. Electrochem. Soc. 1998;145(6): 2051–2057. DOI: 10.1149/1.1838596

[22] Matsumoto K. Enhancement of critical current density of YBCO films by introduction of artificial pinning centers due to the distributed nano-scaled Y_2O_3 islands on substrates. Physica C. 2004;412–414:1267–1271. DOI: 10.1016/j.physc.2004.01.157

[23] Roca i Cabarrocas P. Plasma enhanced chemical vapor deposition of amorphous, polymorphous and microcrystalline silicon films. J. Non-Cryst. Solids. 2000;266–269:31–37. DOI: 10.1016/S0022-3093(99)00714-0

[24] Roca i Cabarrocas P. Plasma enhanced chemical vapor deposition of silicon thin films for large area electronics. Curr. Opin. Solid State Mater. Sci. 2002;6:439–444. DOI: 10.1016/S1359-0286(02)00112-2

[25] Vladimirov S V, Ostrikov K. Dynamic self-organization phenomena in complex ionized gas systems: new paradigms and technological aspects. Phys. Rep. 2004;393:175–380. DOI: 10.1016/j.physrep.2003.12.003

[26] Nunomura S, Kita M, Koga K, Shiratani M, Watanabe Y. Fabrication of nanoparticle composite porous films having ultralow dielectric constant. Japan. J. Appl. Phys. 2005;44:50–52. DOI: 10.1143/JJAP.44.L1509

[27] Glasner A, Kenat J. The crystallization of KCl from aqueous solutions in the presence of lead ions. I. A calorimetric study. J. Cryst. Growth. 1968;2:119–127. DOI: 10.1016/0022-0248(68)90073-0

[28] Glasner A, Skurnik S. A new mechanism for the crystallization and growth of ionic crystals, with special reference to KCl in the presence of Pb^{2+} ions. Israel J. Chem. 1968;6:69–72. DOI: 10.1002/ijch.196800011

[29] Glasner A, Tassa M. The thermal effects of nucleation and crystallization of KBr and KCl solutions. II. The heat of nucleation and the supersaturated solution. Israel J. Chem. 1974;12:799–816. DOI: 10.1002/ijch.197400069

[30] Glasner A, Tassa M. The thermal effects of nucleation and crystallization of KBr and KCL solutions. III. The heat of crystallization and the co-precipitation of lead ions. Israel J. Chem. 1974;12:817–826. DOI: 10.1002/ijch.197400070

[31] Sunagawa I. Morphology of minerals 'Morphology of Crystals'. Tokyo: Terra Sci. 26 1987:1;511–587.

[32] Sunagawa I. Growth and morphology of diamond crystals under stable and metastable conditions. J. Cryst. Growth. 1990;99:1156–1161. DOI: 10.1016/S0022-0248(08)80100-5

[33] Botsaris G D, Reid R C. Comments on the letter by Glasner and Skurnik entitled 'Growth of potassium chloride crystals from aqueous solutions. I. the effect of lead chloride'. J. Chem. Phys. 1967;47:3689. DOI: 10.1063/1.1712456

[34] Meldrum F C, Cölfen H. Controlling mineral morphologies and structures in biological and synthetic systems. Source of the Document Chemical Reviews. 2008;108:4332–4432. DOI: 10.1021/cr8002856

[35] Niederberger M, Cölfen H. Oriented attachment and mesocrystals: non-classical crystallization mechanisms based on nanoparticle assembly. Phys Chem Chem Phys. 2006;8:3271–3287. DOI: 10.1039/B604589H

[36] Cölfen H, Antonietti M. Mesocrystals: inorganic superstructures made by highly parallel crystallization and controlled alignment. Angew. Chem. – Int. Ed. 2005;44(35): 5576–5591. DOI: 10.1002/anie.200500496

[37] Liao H G, Cui L, Whitelam S, Zheng H. Real-time imaging of Pt_3Fe nanorod growth in solution. Science. 2012;336(6084):1011–1014. DOI: 10.1126/science.1219185

[38] Yuk J M, Park J, Ercius P, Kim K, Hellebusch D J. Crommie M F, Lee J Y, Zettl. High-resolution EM of colloidal nanocrystal growth using graphene liquid cells A. Science. 2012;336(6077):61–64. DOI: 10.1126/science.1217654

[39] Zheng H, Smith R K, Jun Y W, Kisielowski C, Dahmen U. Observation of single colloidal platinum nanocrystal growth trajectories. Science. 2009;324(5932):1309–1312. DOI: 10.1126/science.1172104

[40] Fang Z, Wang H. Densification and grain growth during sintering of nanosized particles. Angew. Chem. 2008;53:326–352. DOI: 10.1179/174328008X353538

[41] Clare B W, Talukder G, Jennings P J, Cornish J C L, Hefter G T. Effect of charge on bond strength in hydrogenated amorphous silicon. J. Comp. Chem. 1994;15(6):644–652. DOI: 10.1002/jcc.540150608

[42] Utke I, Hoffmann P, Melngailis J. Gas-assisted focused electron beam and ion beam processing and fabrication. J. Vac. Sci. Technol. B. 2008;26(4):1197. DOI: 10.1116/1.2955728

[43] Randolph S, Toth M, Cullen J, Chandler C, Lobo C. Kinetics of gas mediated electron beam induced etching. Appl. Phys. Lett. 2011;99(21):213103. DOI: 10.1063/1.3662928

[44] Lobo C J, Martin A, Phillips M R, Toth M. Electron beam induced chemical dry etching and imaging in gaseous NH_3 environments. Nanotechnology. 2012;23(37):375302. DOI: 10.1088/0957-4484/23/37/375302/meth

[45] Zheng H, Liu Y, Mao SX, Wang J, Huang J Y. Beam-assisted large elongation of in situ formed Li_2O nanowires. Scientif. Rep. 2012;2:542. DOI: 10.1038/srep00542

[46] Shan Z, Adesso G, Cabot A, Sherburne M, Asif S S, Warren O, Chrzan D, Minor A. Ultrahigh stress and strain in hierarchically structured hollow nanoparticles. Nat. Mater. 2008;7(12):947–952. DOI: 10.1038/nmat2295

[47] Shan Z, Li J, Cheng Y, Minor A, Asif S S, Warren O, Ma E. Plastic flow and failure resistance of metallic glass: insight from in situ compression of nanopillars. Phys. Rev. B. 2008;77(15):155419. DOI: 10.1103/PhysRevB.77.155419

[48] Derjaguin B V, Fedoseev D B. The Growth of Diamond and Graphite from the Gas Phase. Moscow: Nauka; 1989. pp. 131–248 DOI: 10.1016/0257-8972(89)90129-1

[49] Spitsyn B V, Bouilov L L, Derjaguin B V. Vapor growth of diamond on diamond and other surfaces. J. Cryst. Growth. 1981;52(1):219–226. DOI: 10.1016/0022-0248(81)90197-4

[50] Matsumoto S, Sato Y, Tsutsumi M, Setaka N. Growth of diamond particles from methane-hydrogen gas. J. Mater. Sci. 1982;17(11):3106–3112. DOI:http://dx.doi.org/10.1143/JJAP.21.L183

[51] Spear K E. Diamond—ceramic coating of the future. J. Am. Ceram. Soc. 1989;72(2):171–191. DOI: 10.1111/j.1151-2916.1989.tb06099.x

[52] Angus J C, Hayman C C. Low-pressure, metastable growth of diamond and 'diamond like' phases. Science. 1988; 241(4868):913-921. DOI : http://search.proquest.com/docview/213537217?accountid=6802

[53] Kamo M, Sato Y, Matsumoto S, Setaka N. Diamond synthesis from gas phase in microwave plasma. J. Cryst. Growth. 1983;62(3):642–644. DOI: 10.1016/0022-0248(83)90411-6

[54] Haubner R, Lux B. Diamond growth by hot-filament chemical vapor deposition: state of the art. Diamond Relat. Mater. 1993;2(9):1277–1294. DOI: 10.1016/0925-9635(93)90008-P

[55] Belokurov B V. Isotropic surface energies of diamond. Zh. Fiz. Khim. 1960;34:440

[56] Fedosayev D V, Deryagin B V, Varasavskaja I G. The growth of diamond and graphite from the gas phase. Surf. Coat. Technol. 1989;38(1–2):131–248. DOI: 10.1016/0257-8972(89)90129-1

[57] Choi K, Kang S J L, Jang H M, Hwang N M. Nucleation behavior in the presence of charge in the CVD diamond process. J. Cryst. Growth. 1997;172(3–4):416–425. DOI: 10.1016/S0022-0248(96)00759-2

[58] Hwang N M, Bahng G W, Yoon D N. Thermodynamics and kinetics for nucleation of diamond in the chemical vapor deposition process. Diamond Relat. Mater. 1992;1(2–4):191–194. DOI: 10.1016/0925-9635(92)90023-H

[59] Gaskell D R. Introduction to the Thermodynamics of Materials. Washington, DC: Taylor and Francis; 1995. DOI: 10.1016/j.msea.2008.06.016

[60] Jeon J D, Park C J, Kim D Y, Hwang N M. Effect of methane concentration on size of charged clusters in the hot filament diamond CVD process. J. Cryst. Growth. 2001;223:6. DOI: 10.1016/S0022-0248(00)00358-4

[61] Huh J M, Yoon D Y, Kim D Y, Hwang N M. Effect of substrate materials in the low-pressure synthesis of diamond: approach by theory of charged clusters. Z. Metallk. 2005;96(3):225–232. DOI: 10.3139/146.101024

[62] Yang Q, Tang Y, Yang S L, Li Y S, Hirose A. Simultaneous growth of diamond thin films and carbon nanotubes at temperatures ⊛550 °C. Carbon. 2008;46(4):589–595. DOI: 10.1016/j.carbon.2008.01.005

[63] Lee J I, Hwang N M. Generation of negative-charge carriers in the gas phase and their contribution to the growth of carbon nanotubes during hot-filament chemical vapor deposition. Carbon. 2008;46(12):1588–1592. DOI: 10.1016/j.carbon.2008.07.006

[64] Youn W K, Lee S S, Lee J Y, Kim C S, Hwang N M, Iijima S. Comparison of the deposition behavior of charged silicon nanoparticles between floating and grounded substrates. J. Phys. Chem. C. 2014;118(22):11946–11953. DOI: 10.1021/jp5001144

[65] Kim C S, Youn W K, Hwang N M. Generation of charged nanoparticles and their deposition during the synthesis of silicon thin films by chemical vapor deposition. J. Appl. Phys. 2010;108(1):014313. DOI: 10.1063/1.3452352

[66] Chung Y B, Lee D K, Lim J S, Hwang N M. Reduction of amorphous incubation layer by HCl addition during deposition of microcrystalline silicon by hot-wire chemical

vapor deposition. Sol. Energy Mater. Sol. Cells. 2011;95(1):211–214. DOI: 10.1016/j.solmat.2010.04.021

[67] Kumomi H, Yonehara T, Nishigaki Y, Sato N. Selective nucleation based epitaxy (sentaxy): investigation of initial nucleation stages. Appl. Surf. Sci. 1990;41–42:638–642. DOI: 10.1016/0169-4332(89)90135-9

[68] Wagner R S, Ellis W. C. Vapor-liquid-solid mechanism of single crystal growth. Appl. Phys. 1964;4:89–90. DOI:http://dx.doi.org/10.1063/1.1753975

[69] Zhang R Q, Lifshitz Y, Lee S T. Oxide-assisted growth of semiconducting nanowires. Adv. Mater. 2003;15:635–640. DOI: 10.1002/adma.200301641

[70] Roca i Cabarrocas P, Djeridane Y, Bui V D, Bonnassieux Y, Abramov A. Critical issues in plasma deposition of microcrystalline silicon for thin film transistors. Solid-State Electron. 2008;52(3):422–426. DOI: 10.1016/j.sse.2007.10.028

[71] Youn W K, Kim C S, Hwang N M. Effect of the carrier gas flow rate on the microstructure evolution and the generation of the charged nanoparticles during silicon chemical vapor deposition. J. Nanosci. Nanotechnol. 2013;13(10):7127–7130. DOI: 10.1166/jnn.2013.7669

[72] Park S H, Park J W, Yang S M, Kim K H, Hwang N M. Effect of electric bias on the deposition behavior of ZnO nanostructures in the chemical vapor deposition process. J. Phys. Chem. C. 2015:119:25047–25052. DOI: 10.1021/acs.jpcc.5b06796

[73] Davies C N (Ed.). Aerosol Science. New York: Academic; 1966. 1548 p. DOI: 10.1126/science.157.3796.1548-a

[74] Park S H, Park J W, Kim C S, Hwang N M. Formation of tetrapod-shaped nanowires in the gas phase during the synthesis of ZnO nanostructures by carbothermal reduction. J. Nanosci. Nanotechnol. 2013;13:7198–7201. DOI: 10.1166/jnn.2013.7697

[75] Youn W K, Kim C S, Lee J Y, Lee S S, Hwang N M. Generation of charged nanoparticles and their deposition behavior under alternating electric bias during chemical vapor deposition of silicon. J. Phys. Chem. C. 2012;116:25157–25163. DOI: 10.1021/jp310705p

[76] Cheng Q, Xu S. Rapid, low-temperature synthesis of nc-Si in high-density, non-equilibrium plasmas: enabling nanocrystallinity at very low hydrogen dilution. Ostrikov, K. J. Mater. Chem. 2009;19:5134–5140. DOI: 10.1039/B904227J

[77] Hayasaki K, Takamura Y, Yamaguchi N, Terashima K, Yoshida T. Scanning tunneling microscopy of epitaxial $YBa_2Cu_3O_{7-x}$ films prepared by thermal plasma flash evaporation method. J. Appl. Phys. 1997;81:1222. DOI: 10.1063/1.364143

[78] Takamura Y, Hayasaki K, Terashima K, Yoshida T. Cluster size measurement using microtrench in a thermal plasma flash evaporation process. J. Vac. Sci. Technol. B. 1997;15:558. DOI: 10.1116/1.589292

[79] Terashima K, Yamaguchi N, Hattori T, Takamura Y, Yoshida T. High rate deposition of thick epitaxial films by thermal plasma flash evaporation. Pure Appl. Chem. 1998;70:1193–1197. DOI: 10.1351/pac199870061193

[80] Takamura Y, Hayasaki K, Terashima K, Yoshida. High-rate deposition of $YBa_2Cu_3O_{7-x}$ films by hot cluster epitaxy. J. Appl. Phys. 1998;84:5084. DOI: 10.1063/1.368757

[81] Yamaguchi N, Sasajima Y, Terashima K, Yoshida T. Molecular dynamics study of cluster deposition in thermal plasma flash evaporation. Thin Solid Films. 1999;345:34–37. DPI:10.1016/S0040-6090(99)00074-7

[82] Yoo S W, Hong J S, Lee S S, Kim C S, Kim T, Hwang N M. Nonclassical crystallization in low-temperature deposition of crystalline silicon by hot-wire chemical vapor deposition. Cryst. Growth Des. 2014;14(12):6239–6247. DOI: 10.1021/cg5008582

[83] Chung Y B, Lee S H, Bae S H, Park H K, Jung J S, Hwang N M. Effect of the initial structure on the electrical property of crystalline silicon films deposited on glass by hot-wire chemical vapor deposition. J. Nanosci. Nanotechnol. 2012;12:5947–5951. DOI: 10.1166/jnn.2012.6415

[84] Lee S S, Ko M S, Kim C S, Hwang N M. Gas phase nucleation of crystalline silicon and their role in low-temperature deposition of microcrystalline films during hot-wire chemical vapor deposition. J. Cryst. Growth. 2008;310;3659–3662. DOI: 10.1016/j.jcrysgro.2008.05.009

[85] Krishnan A T, Bae S, Fonash S J. Low temperature microcrystalline silicon thin film resistors on glass substrates. Solid State Electron. 2000;44:1163–1168. DOI: 10.1016/S0038-1101(00)00057-5

[86] Persidis E, Baur H, Pieralisi F, Schalberger P, Fruehauf N. Area laser crystallized LTPS TFTs with implanted contacts for active matrix OLED displays. Solid State Electron. 2008;52:455–461. DOI: 10.1016/j.sse.2007.10.014

[87] Shah A, Torres P, Tscharner R, Wyrsch N, Keppner H. Photovoltaic technology: the case for thin-film solar cells. Science. 1999;285:692–698. DOI: 10.1126/science.285.5428.692

[88] Uchikoga, Ibaraki N. Low temperature poly-Si TFT-LCD by excimer laser anneal. Thin Solid Films. 2001;383:19–24. DOI: 10.1016/S0040-6090(00)01644-8

[89] Kahn H, Tayebi N, Ballarini R, Mullen R, Heuer A. Sens. Fracture toughness of Polysilicon MEMS devices. Actuators A – Phys. 2000;82:274–280. DOI: 10.1016/S0924-4247(99)00366-0

[90] Shimoda T, Matsuki Y, Furusawa M, Aoki T, Yudasaka I, Tanaka H, Iwasawa H, Wang D, Miyasaka M, Takeuchi Y. Solution-processed silicon films and transistors. Nature. 2006;440:783–786. DOI: 10.1038/nature04613

[91] Jang J, Oh J Y, Kim S K, Choi Y J, Yoon S Y, Kim C O. Electric-field-enhanced crystallization of amorphous silicon. Nature. 1998;395:481–483. DOI: 10.1038/26711

[92] Morimoto R, Izumi A, Masuda A, Matsumura H. Low-resistivity phosphorus-doped polycrystalline silicon thin films formed by catalytic chemical vapor deposition and successive rapid thermal annealing. Jpn. J. Appl. Phys. 2002;41:501–506. DOI: 10.1143/JJAP.41.501

[93] Matsumura H. Summary of research in NEDO Cat-CVD project in Japan. Thin Solid Films. 2001;395:1–11. DOI: 10.1016/S0040-6090(01)01198-1

[94] Mahan A H. Status of Cat-CVD (Hot Wire CVD) research in the United States. Thin Solid Films. 2001;395:12–16. DOI: 10.1016/S0040-6090(01)01199-3

[95] Schropp R E I. Status of Cat-CVD (Hot-Wire CVD) research in Europe. Thin Solid Films. 2001;395:17–24. DOI: 10.1016/S0040-6090(01)01200-7

[96] Roca i Cabarrocas P, Fontcuberta i Morral A, Kalache B, Kasouit S. Microcrystalline silicon thin-films grown by plasma enhanced chemical vapour deposition -growth mechanisms and grain size control. Solid State Phenom. 2003;93:257–268. DOI: 10.4028/www.scientific.net/SSP.93.257.

[97] Chung Y B, Lee D K, Kim C S, Hwang N M. Effect of HCl addition on the crystalline fraction in silicon thin films prepared by hot-wire chemical vapor deposition. Vacuum. 2009;83:1431–1434. DOI: 10.1016/j.vacuum.2009.05.004

[98] Chung Y B, Park H K, Lee S H, Song J H, Hwang N M. N-type crystalline silicon films free of amorphous silicon deposited on glass by HCl addition using hot wire chemical vapour deposition. J. Nanosci. Nanotechnol. 2011;11:8242–8245. DOI: 10.1166/jnn.2011.5040

[99] Hwang N M. Deposition and simultaneous etching of Si in the chemical vapor deposition (CVD) process: approach by the charged cluster model. J. Cryst. Growth. 1999;205:59–63. DOI: 10.1016/S0022-0248(99)00247-X